JGR Solid Earth

RESEARCH ARTICLE
10.1029/2023JB028361

Frictional Contacts Between Rough Grains With Fractal Morphology

Deheng Wei[1,2,3], Chongpu Zhai[1], Hengxu Song[4,5], Ryan Hurley[6,7], Shaoqi Huang[1], Yixiang Gan[3], and Minglong Xu[1]

[1]State Key Laboratory for Strength and Vibration of Mechanical Structures, School of Aerospace Engineering, Xi'an Jiaotong University, Xi'an, China, [2]Key Laboratory of Ministry of Education on Safe Mining of Deep Mines, School of Resources and Civil Engineering, Northeastern University, Shenyang, China, [3]School of Civil Engineering, The University of Sydney, Sydney, NSW, Australia, [4]State Key Laboratory of Nonlinear Mechanics, Institute of Mechanics, Chinese Academy of Sciences, Beijing, China, [5]School of Engineering Science, University of Chinese Academy of Sciences, Beijing, China, [6]Hopkins Extreme Materials Institute, Johns Hopkins University, Baltimore, MD, USA, [7]Department of Mechanical Engineering, Johns Hopkins University, Baltimore, MD, USA

Key Points:

- Transverse contacts are simulated between two fractal rough grains generated by ultra-high degree spherical harmonics for the first time
- Cattaneo-Mindlin solution is extended to the full slide regime, capable of predicting the critical partial-to-complete sliding transition
- Effects of roughness can be generally neutralized by plasticity, high contact interference, and friction coefficient

Correspondence to:
C. Zhai and M. Xu,
zhaichongpu@xjtu.edu.cn;
mlxu@mail.xjtu.edu.cn

Citation:
Wei, D., Zhai, C., Song, H., Hurley, R., Huang, S., Gan, Y., & Xu, M. (2024). Frictional contacts between rough grains with fractal morphology. *Journal of Geophysical Research: Solid Earth*, *129*, e2023JB028361. https://doi.org/10.1029/2023JB028361

Received 30 NOV 2023
Accepted 21 SEP 2024

Author Contributions:
Conceptualization: Deheng Wei, Chongpu Zhai, Hengxu Song, Ryan Hurley, Minglong Xu
Data curation: Deheng Wei, Chongpu Zhai
Formal analysis: Deheng Wei, Chongpu Zhai, Hengxu Song, Yixiang Gan
Funding acquisition: Deheng Wei, Chongpu Zhai, Minglong Xu
Investigation: Deheng Wei, Chongpu Zhai, Hengxu Song, Ryan Hurley, Shaoqi Huang, Yixiang Gan, Minglong Xu
Methodology: Deheng Wei, Chongpu Zhai, Hengxu Song, Minglong Xu
Project administration: Chongpu Zhai, Minglong Xu
Resources: Deheng Wei, Chongpu Zhai, Minglong Xu
Software: Deheng Wei, Chongpu Zhai, Hengxu Song, Minglong Xu
Supervision: Chongpu Zhai, Hengxu Song, Ryan Hurley, Yixiang Gan, Minglong Xu
Validation: Deheng Wei, Chongpu Zhai, Hengxu Song, Ryan Hurley, Shaoqi Huang

Abstract Surface morphology plays a crucial role in friction between two contacting geomaterial surfaces, yet many questions remain unanswered regarding how detailed frictional responses deviate from analytical solutions for smooth surfaces due to the presence of roughness. In this study, we revisit the Cattaneo-Mindlin problem for contacts between two fractally rough elastic or elasto-plastic spheres generated based on ultra-high degree (e.g., up to 2,000) spherical harmonics with the corresponding wavelength less than a thousandth of the mean grain diameter. Transverse contacts are simulated by finite element method, validated by the extended Cattaneo-Mindlin solution to full slide regime for smooth sphere contacts. Extensive simulations are conducted to study contacts between two rough spheres with various surface geometries, micro friction coefficients, normal contact distances, relative roughness, fractal dimensions, and wavelength ranges. Out results indicate that: (a) the new analytical solution can approximately predict the macro contact response except for extremely high relative roughness and narrow wavelength range; (b) deviations induced by roughness from smooth sphere contacts can be neutralized by plasticity, high normal contact interference, and high micro friction coefficient; and (c) fractal dimension impacts frictional contacts less than relative roughness. The main cause of these phenomena can be credited to the underlying microscale contact information. Contact area and stress distributions and their evolutions provide concrete evidence of these observed behavior. This work provides a pathway for applying computational contact mechanics to many geophysical fields, such as the asperity model in earthquake science and the mechanics of granular materials.

Plain Language Summary Geophysical bodies, such as faults, rocks, and grains, exhibit surface roughness across length scales. Contacts between rough surfaces are usually simplified to a rough-to-flat contact scenario. To release these strong assumptions, for the first time, extensive finite element simulations are conducted for transverse contacts between two rough grains. Particularly, grain roughness is controlled by ultra-high degree spherical harmonics, which enables depicting surfaces of diverse grains from silica sands up to asteroids. Our results highlight the importance of surface features in frictional contacts, and indicate that the effects of roughness can be alleviated by the plasticity, contact conditions, and high intrinsic friction coefficient. Furthermore, fractality, quantifying how much the surface fluctuates over length scales, impacts frictional contacts less than roughness amplitude. This study provides a pathway for applying computational contact mechanics to many geophysical applications involving frictional contacts, such as asperity models in earthquake science and mechanics of granular materials.

1. Introduction

Surfaces of geological materials, such as sand grains, rocks, and faults, usually present roughness over several orders of magnitude of length scales (Candela et al., 2012). Assessing what happens on the interface between such two rough surfaces is crucial for diverse geophysical applications, and has become a focal point of earthquake science in recent years, especially with the rapid development of experimental and numerical capacity and accuracy. Contact mechanics of rough surfaces considering asperity shape, size, and position can be traced back to the pioneering work by Greenwood and Williamson (1966) for open half space, and Greenwood and Tripp (1967)

Visualization: Deheng Wei
Writing – original draft: Deheng Wei
Writing – review & editing: Deheng Wei, Chongpu Zhai, Hengxu Song, Ryan Hurley, Shaoqi Huang, Yixiang Gan, Minglong Xu

for closed curve surface. These analytical solutions are for purely elastic material with individual asperity deemed a half ellipsoidal cap (Bush et al., 1975), enabling the application of classical Hertzian contact solution (Hertzian, 1881). The complex morphologies of the contacting surfaces are often considered with simplified parameters, such as fractal dimension, root mean square roughness, asperity density and average radius, and these multi-asperity models (Carbone & Bottiglione, 2008; Ciavarella et al., 2006; Kadin et al., 2006; Nayak, 1971; Xu et al., 2022) in line with the classical GW model only performs well at short contact interference. B. N. Persson (2006) proposed a contact theory based on the concept of magnification, where rough surfaces are considered to demonstrate gradual evolutions down to fine scales, thus the overall contact is a sum of contacts at every magnification. This treatment is based on the assumption that the interface is fully contacted, which is more accurate for contact problems with large contact interference. It is worthwhile to mention that Guo et al. (2019) unified solutions of classical GW model and Persson's theory, which have been validated by results of molecular dynamics (MD) from Yang and Persson (2008a, 2008b) and experiments from Lorenz et al. (2010) and Lorenz (2012). Most of the aforementioned models originated from contact mechanics have been widely adopted for the contact between the inhomogeneous in geophysical research, that is, the Hertzian contact for acoustic waves in granular materials (Melosh, 1979), and GW theory for rock fracture or joint contact related phenomenon including closure (Brown & Scholz, 1985b; Walsh & Grosenbaugh, 1979), porosity influenced conductivity (Walsh & Brace, 1984), and anisotropic force-deformation behavior (Misra, 1999). The more recently proposed Persson theory has also been utilized to investigate the bulk compressibility of Bentheim sandstone (L. Wang et al., 2020) and the aperture-determined permeability of discrete fracture networks (De Dreuzy et al., 2012).

Additionally, existing analytical contact models mostly depart from the strong assumption that the contact between two non-adhesive elastic frictionless rough surfaces can be deemed as the contact between one rigid flat and one rougher surface with the same composite roughness and elastic modulus (Barber, 2003). If $z_{i,j}$ is the height over the arithmetic mean of nominally flat surface at the position of (i, j), the composite roughness ($z_{c_{ij}}$) is defined as: $z_{c_{ij}} = z_{\mathbb{l}_{ij}} + z_{\mathbb{u}_{ij}}$, where the subscript $\mathbb{l}$ and $\mathbb{u}$ represent "lower" and "upper" surfaces, respectively. These factors conceptually block the application of analytical methods to frictional rough-rough contact rich in asperity interplay like squeezing, plowing, and sliding (Molinari et al., 2018; Song et al., 2015). The direct evidence is experimentally dedicated by Hsu et al. (2018), wherein the friction coefficient at the contact between a rough sphere and a rough flat is much different from that of identical composite roughness between a smooth sphere and a rougher flat. Such a strong assumption could be more ill-posed in geophysical applications, as in this field the surfaces on which the contact is focused are mainly formed from the two sides of the fractured bulk; the contacted surfaces are nearly mated over specific wavelength (Brown & Scholz, 1985a). In the manner of approximating fractured surface height variations using a sum of the Fourier series (Brown & Scholz, 1985b), the distance, over which sine and cosine waves at the specific Fourier series degree repeat, is called wavelength. Via this simplification, the tortuosity of apertures is compressed into $z_{c_{ij}}$, which is short and could lead to a large tortuosity. Certainly, in this framework the permeability prediction is not rigorous. As early in 1994, Yoshioka (1994) has noticed the disagreements with and without the simplifications in geophysical problems, that is, elastic behavior between contacting rough surfaces. Up to now, analytical solutions are still facing challenges to appropriately incorporate deformations and the interplay among asperities (Afferrante et al., 2012; S. Li et al., 2018), with further difficulties when (size-dependent) plasticity (Song et al., 2016, 2017) comes into play. Further, analytical solutions suffer from the geometrical coupling between the normal and tangential elastic field for the contact between two dissimilar surfaces. For such situations, numerical simulations, such as finite element methods (FEM) in this study, are one of effective tools currently available to fundamentally study friction between two deformable bodies.

Moreover, only a few studies focused on friction contact between isotropically rough surfaces, which is more urgent considering that most geomaterial surfaces are of, if not completely, highly isotropic fractality. These existing studies mainly consider materials with rheological behavior, such as viscoelasticity (Putignano et al., 2019) and adhesion (Lengiewicz et al., 2020; Sahli et al., 2019). Strong anisotropy is observed in the deformation and displacements of contact clusters, and the anisotropy is found to be linked to differences between leading and trailing edges of microcontacts (Sahli et al., 2019). In most friction-related studies, the contact area is the main "state variable." However, it is widely admitted that tracking contact area is insufficient in depicting friction-related phenomena (Q. Li et al., 2011), Dillavou and Rubinstein (2018, 2020) challenged the traditional equivalence between contact area and static friction coefficient by experimentally showing that a static shear load could accelerate frictional aging rather than the aging rate of the real contact area. More information at the

microscale, such as normal contact and frictional forces or stresses, deserves more attention. This information is difficult to obtain in experiments, but conveniently achieved in numerical modeling.

First-principles calculations of frictional forces for realistic systems are generally impossible. The reason is that friction is usually an interfacial property, often determined by the last few uncontrolled monolayers of atoms or molecules at the interface. Thus, in continuum scale simulations some *ad-hoc* empirical laws at both the interface and the bulk (such as the minimal case of Amonton-Coulomb friction and isotropic elasticity) must be dedicated to the underlying mechanisms inherent in the studied frictional contacts. Among these simplifications for frictional contact problems, partial-to-full sliding between two identical elastic smoothed spheres with the Coulomb type friction is one of the most concerning problems for its fundamental analogy to real contact behavior. The very first analytical solution to this end was developed, independently, by Cattaneo (1938) and Mindlin (1949). They derived the model for the partial-to-full sliding evolution at the contact between two elastic spheres, referring to Hertzian solution (Hertzian, 1881) for the normal compression. During the tangential motion, the stick zone formed by normal contact pressure shrinks from its circular edge of lower stress, while the slide zone evolves in an annulus shape from this edge toward the contact center and finally occupies the whole contact region, after which the full slide starts. The linear elastic material enables the calculation of the shear traction distribution by superposition of two solutions: one is for limiting frictional traction distribution; the other is a negative correction equal to the product of dry Coulomb friction coefficient and normal contact pressure distribution on the evolutionary stick zone. Later on, more complicated loading scenarios with varying normal and tangential forces have been studied by Mindlin and Deresiewicz (1953). More generalized results on contact geometry have been achieved by Jäger (1995, 1998), independently followed by Ciavarella (1998a, 1998b). The Cattaneo-Mindlin problem has attracted significant attention from geophysical disciplines, such as the asperity model in earthquake science (Beck & Ruff, 1984; Gao, 1989) and discrete element method (DEM) in granular materials (Cundall & Strack, 1979). However, the full slide regime following the partial slide regime, in the contact between two finite sized spheres, has been seldom studied. Moreover, as aforementioned simplifying an asperity contact to a spherical contact with an effective radius significantly eases the analytical investigations on contacts between rough surfaces; at the same time, the simplification might be too ideal to deal with practical problems where roughness is inevitable on both surfaces of contact pairs, and on different length scales. Thus, it is of great importance to study partial-to-full slide behavior between two rough spheres, especially considering the fractal nature of the roughness instead of GW type roughness on a single-length scale.

In this paper, we first extended the Cattaneo-Mindlin solution to full slide regime for smooth sphere contacts; then it was validated by FEM simulations and compared with contacts between two rough spheres of various simulation parameters. To the best of our knowledge, the partial-to-full sliding behavior between two deformable, isotropically rough spheres with multiscale (fractal) roughness features is numerically studied for the first time. The effect of the roughness and elasto-plastic material properties on the macroscopic frictional responses was systematically investigated, focusing on the departures from smooth sphere contacts. In this study, von Mises plasticity is implemented due to its simple formulations and extensive applications in geomaterials (Borja, 2013). The reasons for considering plasticity in geomaterials can be categorized into three aspects: (a) nearly all macro geomaterials are highly heterogeneous composites, such as sandy soils (comprising over 90% of quartz), which exhibit extensive internal microcracks. Inelastic deformations are primarily caused by the formations of new microcracks and sliding motions within them; (b) in nature, geomaterial surfaces are typically coated with clayey soils, leading to significant plastic deformations at the same contact point only after several rounds of cyclic normal compression between two silica sand particulates (Kasyap et al., 2021); (c) the mechanical deformation behavior of each component in rock composites could be described by the plasticity model (Sly et al., 2023). In our FEM simulations for rough sphere contacts the stress in some elements could approach the yield point. The remainder of this paper is organized as follows. In Section 2, the Cattaneo-Mindlin solution for frictional contact between two smooth elastic spheres is extended to full slide regime. Section 3 is for a detailed description of the FEM scheme. Therein, how to generate a fractal-shaped sphere using ultra-high degree spherical harmonics (SH), as well as its FEM mesh, is first given. Mutual verifications between the FEM framework and the extended Cattaneo-Mindlin solution are subsequently conducted via comparing results from numerical and analytical approaches. Simulation results of contact and sliding between two rough spheres focused on gigantic dominant factors are given in Section 4. A discussion of the asperity micromechanics at the macro contact interface, as well as some geophysical applications, is made in Section 5 and conclusions are summarized in Section 6.

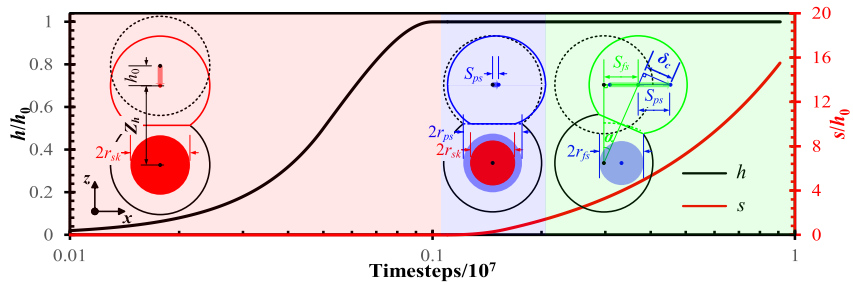

Figure 1. Schematic of the boundary conditions for the extended Cattaneo-Mindlin problem under constant normal contact distance. The two spheres are first compressed to a normal displacement h_0 followed by a tangential shear of displacement s under constant normal displacement. The insets show the typical contact configuration during different regimes. The subscripts "*sk*," "*ps*," and "*fs*" mean stick, partial sliding, and full sliding, respectively. R is the radius, Z_h the distance between two sphere centers, and δ_c the evolutionary slide displacement.

2. Extended Cattaneo-Mindlin Problem

In this section, we focus on extending the classical Cattaneo-Mindlin solution to full slide regime under the constant normal contact distance.

The classical Cattaneo-Mindlin problem involves two loading steps: Step 1 is the normal contact process between two spheres while Step 2 is the tangential loading between two spheres while keeping the normal contact force (resulting from Step 1) a constant. Here, instead of the constant normal force F_z, we adopt the boundary condition of a constant contact distance (normal displacement) h_0. The primary reason is that in order to achieve a constant F_z, a feedback loop is required during the tangential loading process when the normal contact force would naturally evolve; by contrast, a constant normal displacement is a parameter easy to control experimentally. Figure 1 schematically shows the quasi-static loading process, including the contact process, tangential loading process (the so-called partial-to-full sliding regime in Cattaneo-Mindlin problem), and the full slide regime (our extension of the Cattaneo-Mindlin problem).

Without loss of generality, classical solutions to the Cattaneo-Mindlin problem are briefly reviewed in Appendix A. There, we also show that Cattaneo-Mindlin solution is still suitable in the partial sliding regime with a constant normal displacement as the boundary condition. The key to analytically solving forces in the full slide regime of contact between elastic spheres is the projection (S_{ps}) of the x axis on evolutionary slide displacement (δ_c) formed in the partial-to-full sliding regime. The overall tangential displacement, s, is the sum of S_{ps} and the subsequent sliding displacement, S_{fs},

$$s = \underbrace{\frac{\delta_c}{\cos\alpha}}_{S_{ps}} + \underbrace{Z_h \cdot \tan\alpha}_{S_{fs}}, \tag{1}$$

where α is the angle between the x axis and the line connected sphere centers in the full slide regime, $Z_h = 2R - h_0$ is the projection of the distance between two spheres on z axis. Note that δ_c always evolves in a direction parallel to the contact plane, as shown in the right inset schematic in Figure 1. The start and the end of the full slide regime can be also indicated by δ_c in addition to s, by

$$\delta_c = \begin{cases} \delta_{su},\ s = \delta_{su} \\ 0,\ s = \sqrt{(2R)^2 - {Z_h}^2} \end{cases}. \tag{2}$$

Here, $\delta_{su} = \mu_s C_M h_0$, where $C_M = \frac{2-\nu}{2(1-\nu)}$ is a function of Poisson's ratio, ν, and called the Cattaneo-Mindlin ratio, is the ultimate tangential slide displacement when the full slide happens, of which details can be found in Appendix A. Evidently, the traction $F_x(s)$ on the upper sphere is related to the normal contact force $N(\alpha)$ on the interface and the projection of z axis on the reaction force of the upper sphere. According to the following set of equilibrium equations,

$$\begin{cases} \sum_{F_x} = F_x(s) - \mu_s N(\alpha)\cos\alpha + N(\alpha)\sin\alpha = 0 \\ \sum_{F_z} = F_z(s) - \mu_s N(\alpha)\sin\alpha - N(\alpha)\cos\alpha = 0 \end{cases}, \tag{3}$$

$F_x(s)$ and $F_z(s)$ can be expressed as

$$\begin{cases} F_x(s) = N(\alpha)\dfrac{\sin(-\alpha+\beta)}{\cos\beta} \\ F_z(s) = N(\alpha)\dfrac{\cos(\alpha-\beta)}{\cos\beta} \end{cases}, \beta = \tan^{-1}\mu_s. \tag{4}$$

When the full slide happens, the overall contact overlap, h, can also be separated into two parts: one (h_{fs}) is induced by the movement of the upper sphere center in the full slide regime; the other (h_{ps}) is induced by the inclination of the contact interface formed in the partial-to-full sliding regime. Thus, we arrive at

$$h = \underbrace{2R - \frac{Z_h}{\cos\alpha}}_{h_{ps}} - \underbrace{\delta_c \cdot \tan\alpha}_{h_{fs}}. \tag{5}$$

To eliminate δ_c, Equations 1 and 5 are combined and then, together with Equation A1, imported into Equation 4,

$$F_x(s) = \underbrace{\frac{4}{3}E^* R^{*\frac{1}{2}}\left[\underbrace{-(s\cos\alpha - Z_h\sin\alpha)\tan\alpha + 2R - \frac{Z_h}{\cos\alpha}}_{h}\right]^{\frac{3}{2}}}_{N}\frac{\sin(-\alpha+\beta)}{\cos\beta},\ s > \delta_{su}. \tag{6}$$

Then combined with Equation A8, the extended Cattaneo-Mindlin solution to the full slide regime is

$$F_x(s) = \begin{cases} \underbrace{\dfrac{4}{3}E^* R^{*\frac{1}{2}} h_0^{\frac{3}{2}}}_{F_z(s)}\mu_s\left[1 - \left(1 - \dfrac{s}{\delta_{su}}\right)^{\frac{3}{2}}\right],\ s \le \delta_{su} \\ \dfrac{4}{3}E^* R^{*\frac{1}{2}}\left[-(s\cos\alpha - Z_h\sin\alpha)\tan\alpha + 2R - \dfrac{Z_h}{\cos\alpha}\right]^{\frac{3}{2}}\dfrac{\sin(-\alpha+\beta)}{\cos\beta},\ s > \delta_{su} \end{cases}. \tag{7}$$

In next sections, the above extended solution in Equation 7 would be validated by FEM simulations. Here, we have to stress that some, but not all, relevant assumptions in Hertzian normal contact and Cattaneo-Mindlin solutions still hold in this study, as our study is an extension of them. For example, we do not limit to two identical elastic spheres by using two contacted rough spheres with the same roughness parameters but diverse roughness; and the shear stress distribution is of no necessity to be everywhere parallel to the displacement. In line with Hertzian normal contact, internal stress is also ignored. The contact and friction models in FEM are outlined in Appendix C2. The Amonton-Coulomb friction law is also used, wherein the shear stress of any slide contact point is equal to the product of a constant coefficient of friction and normal stress, to avoid the unrealistic infinite shear stress at the edge of the contact interface associated with the no slide assumption of tangential loading.

Considerable controversy persists regarding the most suitable friction law in geophysics (Bhattacharya et al., 2022). For example, the two mostly used versions, see the Aging law (Dieterich, 1979) and the Slip law (Ruina, 1983), of common empirical rate and state dependent friction (RSF) law offer opposing views of the importance of slip for friction evolution via defining different state functions. Even the common sense that the

dynamic friction coefficient is smaller than the maximum static friction coefficient is challenged by Scholtz and collaborators (Biegel et al., 1992; Boitnott et al., 1992; W. Wang & Scholz, 1995) who conducted rotary shear tests on granite and found the dynamic friction coefficient is almost identical to the maximum static friction coefficient. This is consistent with the results of direct shear tests on gabbro conducted by Marone and Cox (1994). The difference between the two types of friction stress, called the stress drop, $\Delta\tau_p$, is of significant importance in earthquake science (Madariaga, 1979) and directly involved in calculating seismic moment, M_0, for a circular crack with the radius equal to $\Re$ (Dublanchet et al., 2013): $M_0 = \frac{16}{7}\Delta\tau_p\Re^3$. Note that all above phenomenological friction laws aim to approximate the macro mechanical response, which is a collective behavior of individual contacting asperities on the rough contact interface. Starting from the minimal mode considering only material elasticity and Coulomb friction of single rough asperities (such as the whole rough sphere deemed as one asperity on the rough surface), and progressively incorporating additional mechanisms such as adhesion, fracture, and abrasion, may help elucidate the mismatches among various friction laws.

There are two reasons to adopt the Amonton-Coulomb friction law at specific contact points in our FEM schema: (a) in the classical Cattaneo-Mindlin problem which is aimed to be extended to the post-full-slide regime and rough spheres, the friction force is limited by non-adhesive Amonton-Coulomb friction law; (b) in large-scale molecular simulations in Mo et al. (2009), Amonton-Coulomb friction law is found for non-adhesive contact at single asperity, nevertheless rate and state friction law is found in plenty of single contacts in experimental studies (Q. Li et al., 2011; S. Li et al., 2020). Note that the rate and state friction law, although computationally too much to handle, can be readily imported into the interface contact law in FEM and could influence our results much; in the classical Cattaneo-Mindlin problem of interest in this study, rate and state effects are not considered.

3. Numerical Methods

In this study, we implement FEM to simulate contacts between smooth or rough spheres. All simulation parameters are summarized in Appendix B, while detailed descriptions of FEM model including material properties and contact and friction model, as well as some necessary validations of FEM itself, are provided in Appendix C. The boundary conditions have been schematically illustrated in Figure 1. In Step 1, the higher half of the upper sphere first is constrained to be only able to go down along z direction by a constant acceleration up to half of the desired normal contact distance, followed by a continuous decrease of the velocity down to zero. Then, positions of both two spheres will be kept for a short time of period, for better elimination of inertial effects in explicit FEM scheme (see Figure C3 in Appendix C). Notably, the final normal contact distance, h_0, of rough sphere contact is calculated via distances between their mean radial heights, identical to that of the corresponding smoothed sphere contact, $2R - Z_h$, as shown in Figure 1. During Step 2, the higher half of the upper sphere is only allowed to move toward x direction with the same acceleration and maximum velocity as those of movements toward z direction in Step 1. Then, the upper sphere will tangentially move along a linear trajectory at a constant speed until the separation of the two spheres.

In this section, how rough spheres with isotropic roughness are generated is first illustrated using ultra-high degree Spherical Harmonics (USH), followed by the further implementation in FEM mesh for the balance between computational cost and efficiency to depict enough morphology features. Validations are also provided by comparing FEM results with solutions of smooth sphere contacts both in partial and full sliding regimes.

3.1. Rough Sphere Surface and Finite Element Mesh

At large length scales up to asteroids, SH based spectral analysis has been frequently used to quantify fractal dimension of long-known and newly found asteroids, such as Earth, Moon, Venus, and Mars (Turcotte, 1987), and Bennu (Daly et al., 2020); at small length scales down to particles, SH has also been implemented to measure the morphology features of silica grains, such as various engineering particulates in Figure 2a. Compared with other methods to generate rough flat surfaces, such as the Weierstrass-Mandelbrot function (Ciavarella et al., 2006; Komvopoulos & Yang, 2006) and power spectrum (PS) density (Joe et al., 2018; Monti et al., 2022), the advantage of SH is that the surface roughness built upon an initially smooth sphere. In this study, spheres with isotropic roughness are generated based on USH to depict very fine grain morphology using extremely high SH degrees up to 2,000 with the corresponding wavelength equal to about $0.003\bar{r}$. To bypass the underflow phenomena in the Legendre series in SH function of ultra-high degree, a recursion formula is applied (Wei

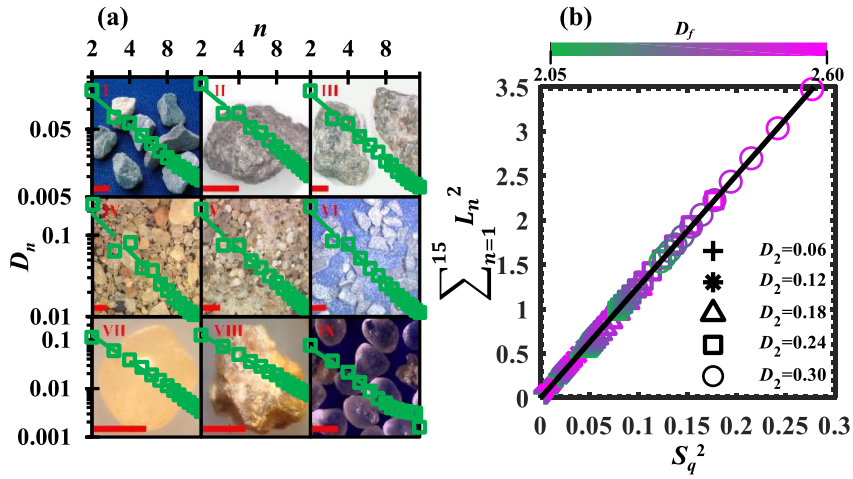

Figure 2. (a) Pictures of nine types of natural grains and the corresponding relations between the average of normalized power spectrum (PS), D_n, and spherical harmonics expansion degree, n, in the log-log scale. Scale bars for I to III and IV to IX are 1 cm and 1 mm. I to VI are MA106A-1, MA107-6, MA114F-3, MA111-7, MA99BC-5, and MA106B-4, taken from Virtual Cement and Concrete Testing Laboratory (Bullard, 2014). VII, Leighton Buzzard sand, and VIII, highly decomposed granite, are from Wei et al. (2018), while IX, Ottawa sand, is from Erdoğan et al. (2017). (b) Relations between the cumulative square of the PS, $\sum_{n=1}^{15} L_n{}^2$, and mean square roughness, $S_q{}^2$, for virtually generated irregular grain shapes of various of D_f and D_2.

et al., 2020), instead. Here we only briefly introduce the key parameters that are varied in this study and newly derive the exact relation between root mean square roughness and PS in SH in Appendix D. All generated fractal rough grains as well as relevant codes are available at our Zenodo repository (Zhai, 2023).

As in Figure 2a, the linear relations between PS, L_n, and SH degree, n, in log-log scale are encountered widely in natural grain shapes, that is, $D_n \propto n^{\beta}$, where D_n is the normalized PS by D_0, $D_n = L_n/D_0$, $\beta = -2H$ is the slope of the regression plot of log (D_n) versus log (n), and H is the Hurst coefficient related to the Fractal Dimension (D_f) of Fourier transformation by the following expression (Russ, 2013):

$$D_f = 3 - H = \frac{6+\beta}{2}. \tag{8}$$

Further, the relative roughness, R_r, indicating how the rough grain is globally distinct from the sphere with the radius equal to the mean radial length, is defined as the ratio of root mean square roughness, S_q, to mean radius length, $\bar{r}$,

$$R_r = \frac{\sqrt{M_{sr}}}{R_0} = \frac{\sqrt{\frac{1}{4\pi}\sum_{n=1}^{\infty}\sum_{m=-n}^{n}\left\|c_n^m\right\|^2}}{c_0^0 \cdot Y_0^0(\theta,\,\varphi)} \approx \frac{S_q}{\bar{r}}. \tag{9}$$

where $\|\cdot\|$ is the L_2 norm, c_n^m are the SH coefficients of degree n and order m, $\theta \in [0,\,\pi]$ and $\varphi \in (0,\,2\pi]$ are the latitudinal and longitudinal coordinates respectively, $Y_n^m(\theta,\,\varphi)$ is the SH function, R_0 is the c_0-determined sphere, and $M_{sr} = S_q{}^2$ is the mean square roughness. Figure 2b demonstrates the consistency between our newly derived relation, between L_n and S_q (see Equation D6 in Appendix D), and results from randomly generated rough grain shapes with various of D_2 and D_f. More details about the way randomness are introduced in the SH for surface generation are provided in Appendix D.

In FEM simulation of the fractal rough surface, the balance between the computational cost and the shortest wavelengths, λ_s, of the rough surface is an important issue as has been intensively discussed in Yastrebov et al. (2012, 2015, 2017a, 2017b). The fractal feature is of course necessarily truncated by the FEM mesh size, ℓ. According to the Jean's formula,

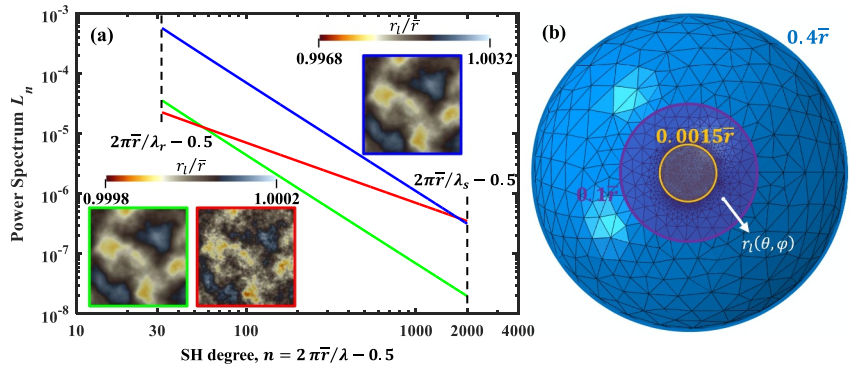

Figure 3. (a) Relations between power spectrum, L_n, and ultra-high degree spherical harmonics degree, n. Inset green, red, and blue plots represent three typical morphology features in mesh-fine zones of $(R_r, D_f) = (2 \times 10^{-5}\sqrt{\pi}, 2.1)$, $(R_r, D_f) = (2 \times 10^{-5}\sqrt{\pi}, 2.5)$, and $(R_r, D_f) = (32 \times 10^{-5}\sqrt{\pi}, 2.1)$, respectively. The former two are for comparing influences of fractal dimension (D_f), while the first and the third are for comparing influences of relative roughness (R_r). Here, $\bar{r}$ denotes the mean radius length, while r_l denotes the lth radius length; $\lambda(n) = \frac{2\pi\bar{r}}{n+0.5}$ is the wavelength and related to n. (b) Graded finite element method mesh for the smoothed sphere. Three circular regimes from the center denote the fine mesh zone, transition zone, and coarse mesh zone, respectively. One set of (θ,φ) represents the latitudinal and longitudinal angle for one point in the spherical coordinate system.

$$\lambda(n) = \frac{2\pi\bar{r}}{n + 0.5}, \tag{10}$$

where $\lambda(n)$ is the wavelength for the waves of degree n for a unit sphere. Ideally, $\lambda(n_{\max}) = \lambda_s \gg \ell$, however, the computational cost limits this application. It would be more rigorous to put $\lambda(n_{\max}) \geq 2\ell$, as suggested in Table 1 in Yastrebov et al. (2015), who summarized the relationship between the shortest wavelength, λ_s and ℓ of recent numerical studies for contact behavior of nominally flat rough surfaces. In this study, we set the ratio $n_{\max} = 2{,}000$.

In order to generate a rough sphere for FEM simulations, a graded spherical surficial triangular mesh is first generated in Matlab environment by distributing surficial nodes on three different mesh zone according to their mesh sizes, including fine mesh zone, transition zone, and coarse mesh zone, as is shown in Figure 3b, of which the FEM mesh is available at our Zenodo repository (Zhai, 2023). The mesh sizes at the boundaries between these three zones are $0.0015\bar{r}$, $0.1\bar{r}$, and $0.4\bar{r}$, respectively. Note that the mesh size transitions gradually from the specified mesh size of the coarse region to that of the fine region. The mesh sizes at the boundaries are exactly the same as the given values. Via this manifestation, $\lambda(n_{\max} = 2,\ 000) = \frac{2\pi}{2,\ 000+0.5} > 0.0015 \times 2$.

The triangular mesh is selected for its strong capability of depicting complicated shapes compared with tetragonal mesh. After initial distribution, the randomly distributed nodes on the sphere surface are moved with iterations for high mesh quality, except for nodes which are fixed and evenly circulated on the boundary between different mesh zones (P. O. Persson & Strang, 2004). By keeping the topology of vertices and just altering their radial length, a rough spherical mesh can be generated via importing their spherical coordinates into Equation 8 (Wei et al., 2020). Insets in Figure 3a depict morphology features of three fractally rough spheres using above steps. After obtaining surface mesh, 3D Delaunay triangulation (Lo, 2014) is implemented to generate tetrahedral elements. Overall, both smoothed and rough spheres have about 90,000 surface and 700,000 volume elements. More than 90% of elements are in the mesh-fine zone. Notably, internal nodes of solid elements of poor quality are also moved with iterations by trials and errors until high-quality elements are achieved. The mesh sensitivity has been analyzed to ensure that the mesh in the contact zone is fine enough; that is if the mesh size is fine enough, with finer mesh the plot depicting normal contact force versus normal contact displacement could remain unchanged, as shown in Figure 1-c. The sign of not fine enough mesh is that the plot of finer mesh size would depart from the original one.

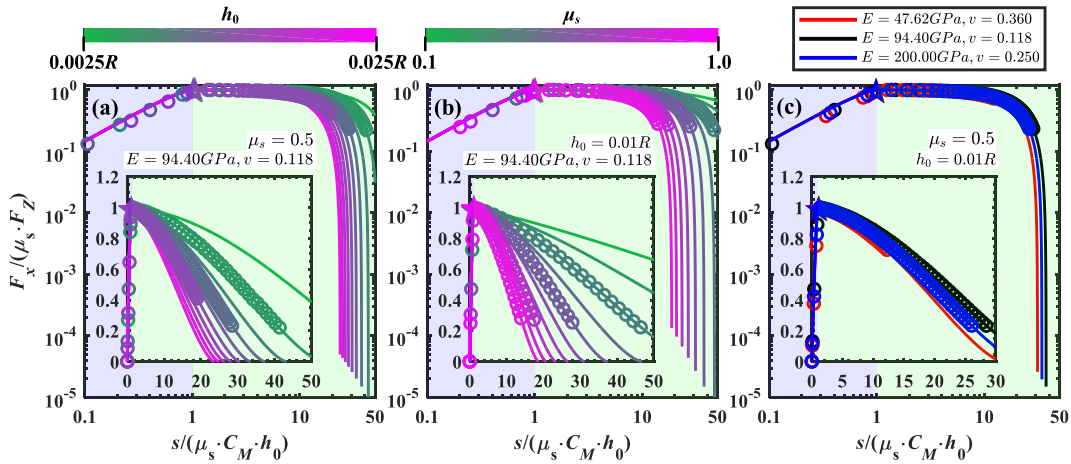

Figure 4. The effects of (a) the normal contact distance, h_0, (b) the Coulomb friction coefficient, μ_s, and (c) material properties on the relationship between the normalized traction forces, $\frac{F_x}{\mu_s F_Z}$, and normalized transverse displacements, $\frac{s}{\mu_s C_M h_0}$ at contacts of two smooth spheres. F_Z is the normal contact force at the end of normal contact just before the start of tangential contact. Solid lines represent analytical results based on the extended Cattaneo-Mindlin solutions, circle points represent finite element method simulation results, and star points represent the transition point from partial sliding to full sliding. The background with the color of transparent blue is for the partial sliding regime, while the color of transparent green is for the full sliding regime.

3.2. Validations of the Extended Cattaneo-Mindlin Solution

We first carry out FEM simulations of friction contacts between two purely elastic smooth spheres. The simulation results are compared with the extended Cattaneo-Mindlin solution (depicting the regime prior to the full slide) to calibrate our FEM simulations, and also to validate the newly derived analytical solution for the full slide regime. The comparison is summarized in Figure 4 for various normal contact distances, friction coefficients, and elastic material properties. Therein, we normalize the tangential displacement by the critical slide displacement, δ_{su}. When the ratio is smaller than one, the transparent blue region in Figure 4 represents the classical regime of the Cattaneo-Mindlin solution (partial-to-full sliding), while it is the full slide regime when the ratio is larger than one, as indicated by the transparent green region. It can be seen in the main plot (in log scale) that our FEM simulation results agree well with the Cattaneo-Mindlin solution, demonstrating the simulation accuracy. In the inset, we can see the consistency between numerical and analytical results for the full slide regime, validating the newly derived analytical solution. Detailed procedures for conducting FEM simulations in Abaqus environments and the function for realizing the extended Cattaneo-Mindlin solution can be found in our Zenodo repository (Zhai, 2023).

4. Results

In this section, influences of plasticity, h_0, μ_s, R_r, and $\lambda_r(n)$ on the tangential contact response for rough spheres are investigated; deviations induced by each factor are discussed by comparing with the reference group (with simulation parameters listed in No. 2–4 of Appendix B and morphology features in mesh-fine zones of bottom surfaces depicted in the insets of Figure 3a). In addition to $F_x(s)$ expressed in Equation 7, $F_z(s)$ is also studied. During the partial-sliding regime, $F_z(s)$ is calculated by Hertzian solution (see Appendix A), while in full slide regime, it can be readily determined by combing Equations 4 and 6,

$$F_z(s) = \begin{cases} \frac{4}{3}E^* R^{*\frac{1}{2}} h_0^{\frac{3}{2}}, \; s \le \delta_{su} \\ \frac{4}{3}E^* R^{*\frac{1}{2}} \left[-(s\cos\alpha - Z_h \sin\alpha)\tan\alpha + 2R - \frac{Z_h}{\cos\alpha} \right]^{\frac{3}{2}} \frac{\cos(\alpha-\beta)}{\cos\beta}, \; s > \delta_{su} \end{cases}. \tag{11}$$

The considered roughness, friction coefficient, normal contact distance, and material properties can be typically seen for grain interactions in diverse geophysical applications (Cavarretta et al., 2011; Y. Li et al., 2021; Otsubo

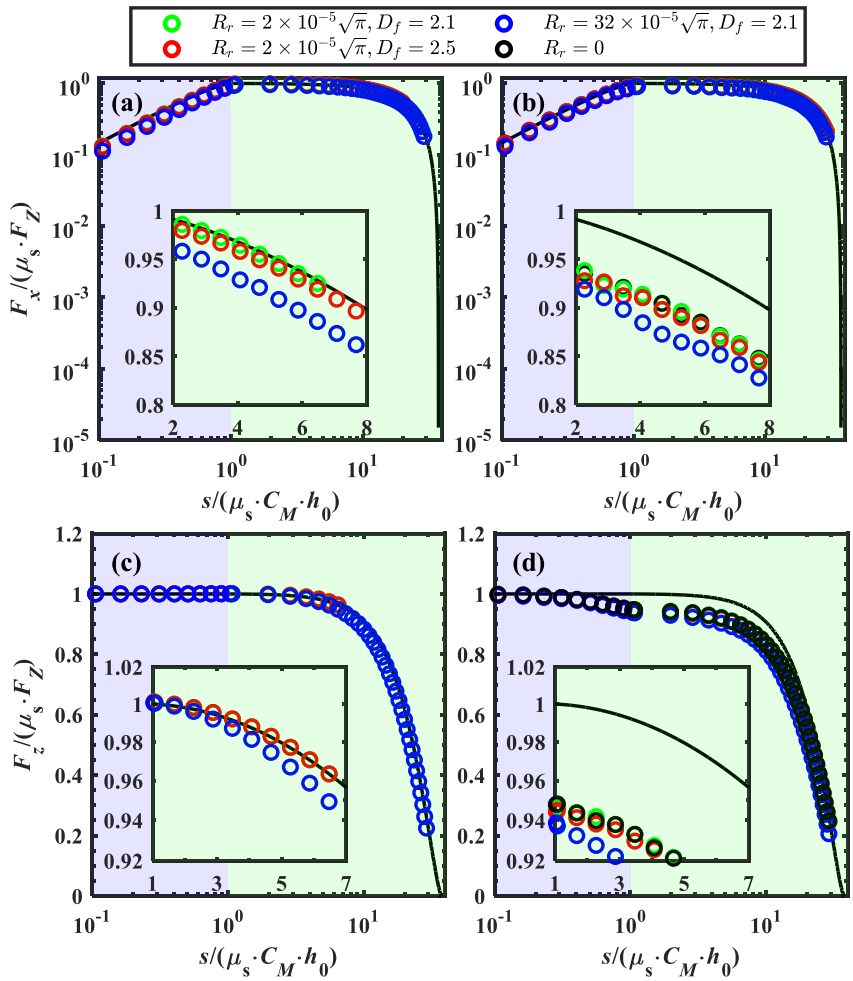

Figure 5. Normalized traction forces, $\frac{F_x}{\mu_s F_Z}$, in (a) and (b) and normalized normal force, $\frac{F_z}{\mu_s F_Z}$ in (c) and (d), versus normalized transverse displacements, $\frac{s}{\mu_s C_M h_0}$, for elastic ((a) and (c) with simulation parameters listed in No. 2–4 of Appendix B) and elasto-plastic contacts ((b) and (d) with simulation parameters listed in No. 25–28 of Appendix B). Solid lines represent analytical solutions of smoothed elastic sphere contacts, while circular points represent simulation results.

& O'Sullivan, 2018), as summarized in Appendix B. Notably, the normal contact distance for rough sphere contact pairs is calculated according to their mean radial lengths, which are the same as their corresponding smoothed spheres.

4.1. Influences of Plasticity

The complete evolutions of the tangential force and vertical force for pure elastic and elasto-plastic contacts during the tangential loading process are shown in Figure 5. The plasticity is represented as a typical isotropic power-law strain hardening, as detailed in Appendix C1. According to some relevant experimental studies of nano indentation on pure components of rock surfaces (Strozewski et al., 2021), the ratio of yield stress σ_Y of pure quartz to the composite elastic E^* denoted in Equation A2 has an order of magnitude about -2. To account for plasticity induced by microcracks and coated clay on the grain surfaces, we set $\sigma_Y = 0.01E^* = 478.66$ MPa. With the hardening constant $\mathcal{K} = 4{,}681.02$ MPa, Equation C6 could represent one linear relation between $\overline{\sigma}$ and ε for both elastic and plastic regimes when the hardening exponent $\eta = 1$. When $\eta = 0$, a perfectly elasto-plastic behavior is represented. Here, $\eta = 0.3$ is utilized for a reference (Ceccato et al., 2022).

No effect on the normalized critical tangential force is observed. Figures 5a and 5c exhibit the effect of the roughness for the purely elastic material. In general, the high roughness results in a smaller critical tangential force and a smaller vertical force at the transition to the full slide regime. The high roughness also leads to a

smaller tangential force from the onset of the applied tangential motion. Figures 5b and 5d show the effect of material plasticity: the critical tangential forces become smaller than that of the elastic contact. Moreover, the effect of the roughness is weakened/neutralized, consistent with results reported by Song et al. (2016). Notably, up to now there is no widely-accepted rigid analytical solution for elasto-plastic smoothed sphere contact, even at the normal contact regime. Thus, to discuss the influence of plasticity on frictional contact, we use results of FEM as a replacement (black lines in Figures 5b and 5d). Interestingly, with the realistic values of $D_f \in (2.1, 2.5)$ and R_r into consideration, negligible differences are found between the case of $D_f = 2.1$ and that of $D_f = 2.5$, especially for F_z; by contrast, high R_r could shift both F_x and F_z more from that of smooth sphere contacts.

It is also noted that when $0 < s \ll \delta_{su}$, the shape of $F_x/(\mu_s \cdot F_Z)$ versus $s/(\mu_s \cdot C_M \cdot h_0)$ for elasto-plastic contact resembles that of elastic contact in the reference group; that is, the tangential response in this stage is less influenced by plasticity. With the increase of s to about $0.2\delta_{su} \lesssim s < \delta_{su}$, F_z drops sharply till $s = \delta_{su}$, while F_z of the elastic sphere contact remains unchanged in the partial-sliding regime. Upon initial inspection of Figure 5d, a question may arise regarding the timing of the transition of slide regimes, particularly as the normal contact force decreases well before $s = \delta_{su}$ for Cases 26–28 detailed in Appendix B. However, this assumption is unfounded. In the classical Cattaneo-Mindlin problem, the transition occurs due to alternations of contact area. While in Figure 5d, the reduction of normal contact force before $s = \delta_{su}$ is attributed to plasticity saturation within the bulk material. As traction stress rises during the sliding process, plasticity saturation intensifies, leading to a decrease in normal contact stress, as shown in Figure 11a. Most importantly, Figure 11a indicates that the entire contact interface remains nearly "static" before $s = \delta_{su}$. When s is increased to $\delta_{su} = \mu_s C_M h_0$, the drop of F_z is alleviated due to the movement of the whole contact interface which stabilizes the bulk plastic saturation to some extent. Furthermore, influences of roughness (say, relative roughness and fractal dimension) induce lower F_x and F_z, which could be compensated by plasticity.

In a pertinent work by Olsson and Larsson (2014), the Coulomb frictional contact between a deformable elasto-plastic sphere and a rigid flat plane with a constant interference was simulated using FEM. They claimed that the initial tangential stiffness, scaled with the elastic prediction from Cattaneo and Mindlin problem, is independent of plasticity, after a careful confirmation that no plastic dissipation was observed during the very initial stage of tangential loading. We extend, here, such an independence on plasticity, responsible for the similar tangential stiffness of elastic contact to elasto-plastic contact, to the contact between two elastic-plastic rough spheres.

4.2. Influences of Normal Contact Distance and Dry Friction Coefficient

There is no doubt that the micro friction coefficient, μ_s, has a significant influence on macro frictional contact response. As early in 1978, Byerlee (1978) in his famous publication, "friction of rocks," summarized a large number of existing experimental data and found that the normal stress (σ_N) determined by normal contact distance dominates the shear stress (τ_f): at low σ_N, $\tau_f = 0.85\sigma_N$, while at high σ_N, $\tau_f = 0.5 + 0.6\sigma_N$, and at extremely high σ_N, $\tau_f = \mathbb{A} \cdot {\sigma_N}^{\mathbb{m}}$, where $\mathbb{A}$ and $\mathbb{m}$ are constants. Since then, the varying normal stress level realized by tunning normal contact distance has been a focal point in geophysics (Kilgore et al., 2017; Linker & Dieterich, 1992).

Figure 6 exhibits the effect of the normal contact distances on the tangential responses, indicating a competition mechanism between normal contact distance and roughness. No effect on the normalized critical tangential force is observed. The larger normal contact distance, h_0, leads to a faster drop of the tangential force in the full slide regimes of both smoothed and rough sphere contacts. As indicated in Figures 6d and 6e, F_z of low-roughness sphere contacts coincides well with that of smooth sphere contacts; however, for high-roughness sphere contacts, in Figure 6f it can be seen that the larger normal load reduces the effect of the roughness through comparisons with smooth sphere contacts. This finding is consistent with the consensus in contact mechanics where the relation between normal contact load and displacement would gradually converge to that of Hertzian solution with the increase of normal load (Pastewka & Robbins, 2016; Pohrt & Popov, 2013; Wei et al., 2020). With this manifestation of normal load, we show here the relationship between normal load and tangential displacement in contacts between two rough elastic spheres can align with that of smooth sphere contacts, even without resorting to the simplification used in previous studies, such as Pohrt and Popov (2013) and Pastewka and Robbins (2016). In those studies, the contact between two rough spheres is approximated as that between an elastic flat substrate and a rigid rougher sphere. Although compared with R_r, D_f has negligible effects on F_z, it alters F_x more as

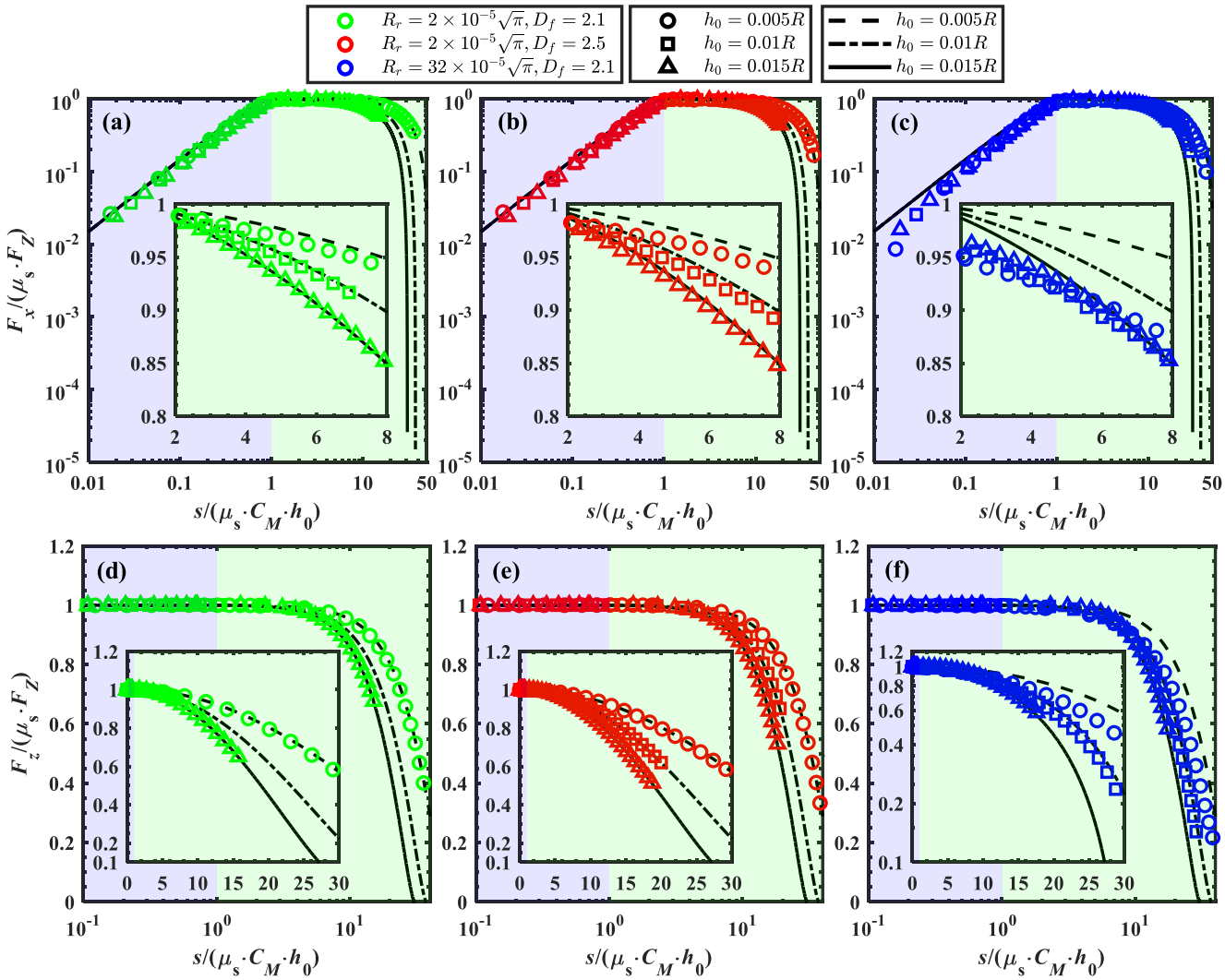

Figure 6. Normalized traction forces, $\frac{F_x}{\mu_s F_Z}$, in (a)–(c) and normalized normal force, $\frac{F_z}{\mu_s F_Z}$ in (d)–(f), versus normalized transverse displacements, $\frac{s}{\mu_s C_M h_0}$, for rough elastic sphere contacts with initial normal displacement h_0 of $0.005R$ (with simulation parameters listed in No. 30–32 in Appendix B), $0.01R$ (with simulation parameters listed in No. 2–4 in Appendix B), and $0.015R$ (with simulation parameters listed in No. 34–36 in Appendix B). Lines represent the extended Cattaneo-Mindlin solutions of smooth spheres, while circular points represent simulation results of rough sphere contacts.

illustrated in Figures 6a and 6b, of which the influences could also be mitigated with the increase of h_0. Such influences of higher h_0 is more evident as demonstrated in Figure 6c, where the discrepancy between rough sphere contact and smooth sphere contact could be highly relieved.

The effect of the pre-defined/micro friction coefficient, μ_s, is shown in Figure 7. No effect on the normalized critical tangential force is observed. The larger micro friction coefficient leads to a faster drop of the tangential force in the full slide regimes of both smoothed and rough sphere contacts. For lower roughness contact, in Figures 7d and 7e relations between normalized F_z and normalized s of rough sphere contacts compare well with those of smooth sphere contacts no matter for higher or lower D_f. Higher D_f could only alter F_x via lower μ_s, as can be seen in Figure 7b. This is because higher μ_s could induce more lateral confining forces on the interfacial surfaces, and thus the wavy surfaces would be more stretched to a "flatter" shape. Consequently, the macro tangential force tends to overlap with that of smooth sphere contacts, of which the contact interface is perfectly flat. Such an explanation is further verified by Figure 7(c), wherein the discrepancy of the curve denoting $F_x/(\mu_s \cdot F_Z)$ versus $s/(\mu_s \cdot C_M \cdot h_0)$ between the higher-rough sphere contact and the corresponding smooth sphere contact of the same μ_s is alleviated gradually with higher μ_s. Meanwhile, the tangential forces of various friction coefficients in rough sphere contact undergo parallel drops to those of corresponding smooth sphere contacts,

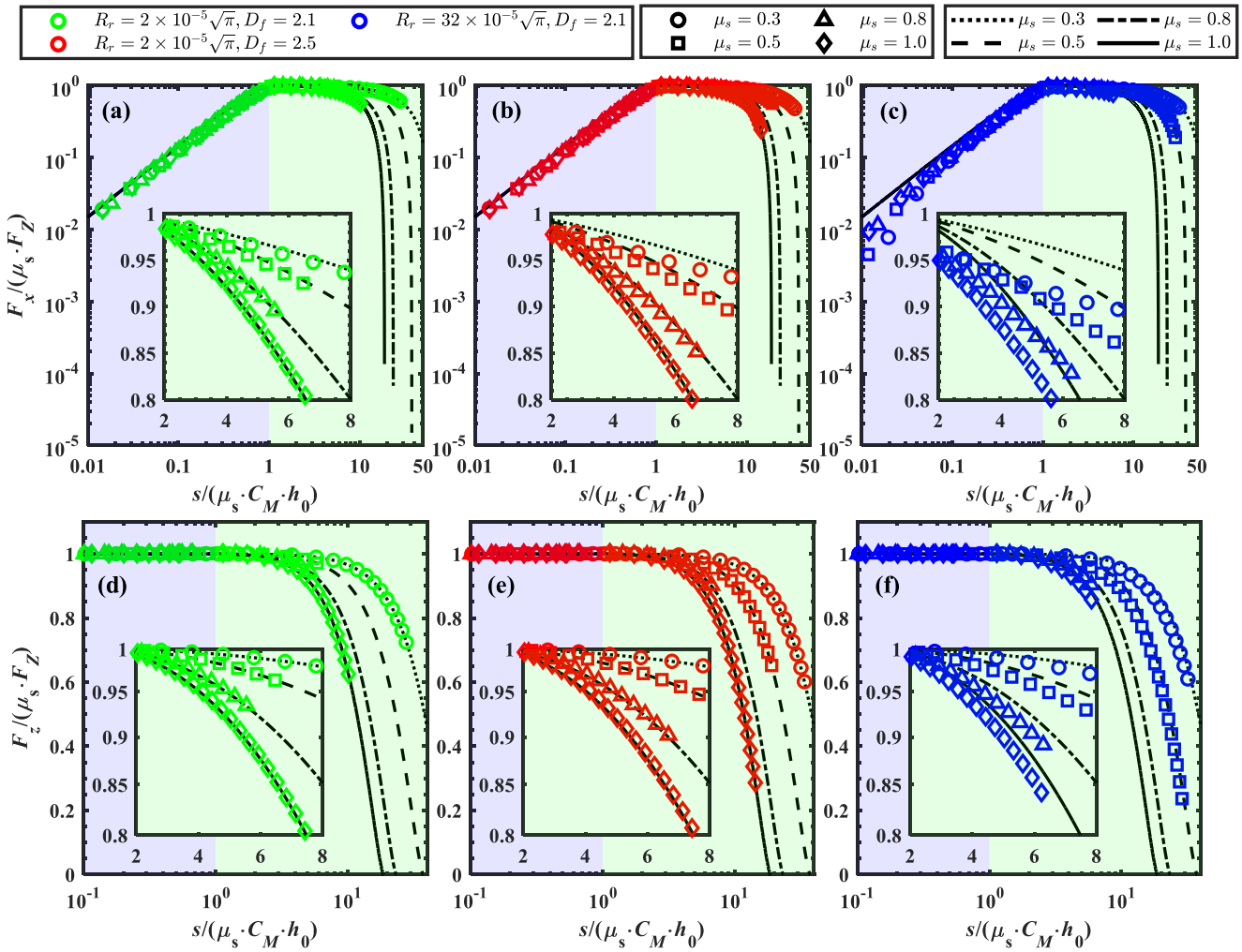

Figure 7. Normalized traction forces, $\frac{F_x}{\mu_s F_Z}$, in (a)–(c) and normalized normal force, $\frac{F_z}{\mu_s F_Z}$ in (d)–(f), versus normalized transverse displacements, $\frac{s}{\mu_s C_M h_0}$, for rough elastic sphere contacts with μ_s of 0.3 (with simulation parameters listed in No. 6–8 in Appendix B), 0.5 (with simulation parameters listed in No. 2–4 in Appendix B), 0.8 (with simulation parameters listed in No. 10–12 in Appendix B) and 1 (with simulation parameters listed in No. 14–16 in Appendix B). Lines represent the extended Cattaneo-Mindlin solutions of smooth spheres, while circular points represent simulation results of rough sphere contacts.

indicating that although there is a competition mechanism between micro friction coefficient and roughness on F_x during the full slide regime, the combined effects of the two factors can be unified and the $F_x - s$ curves retain the shape of smooth sphere contact. By contrast, the discrepancy of F_z does not diminish at all in Figure 7f; that is because F_z is more sensitive to the vertical confining, but μ_s mostly enhance the lateral confining, although the rough sphere has wavy roughness on its surfaces.

4.3. Influences of Relative Roughness

Up to now, roughness is thought to be one of the dominant factors in controlling frictional contact response; exactly speaking, friction coefficient is not a material property, but heavily influenced by loading conditions alternated by changing the contact morphology via only slightly tilting the edges of contacted surfaces (Ben-David & Fineberg, 2011). Albeit this, recent studies by Mollon et al. (2020) have also shown that friction and roughness cannot be taken as equivalent in DEM simulations of biaxial compressions of discrete grains. Specifically, the peak strength of extremely smooth grain samples could saturate and not reach the strength of rough grain samples, no matter how large the micro friction coefficient is specified. This finding not only hinders the application of the experimentally measured friction coefficient (Sandeep et al., 2019) into smooth-contact DEM, but also indicates the sought-after necessity to explicitly introduce roughness in numerical methods. This

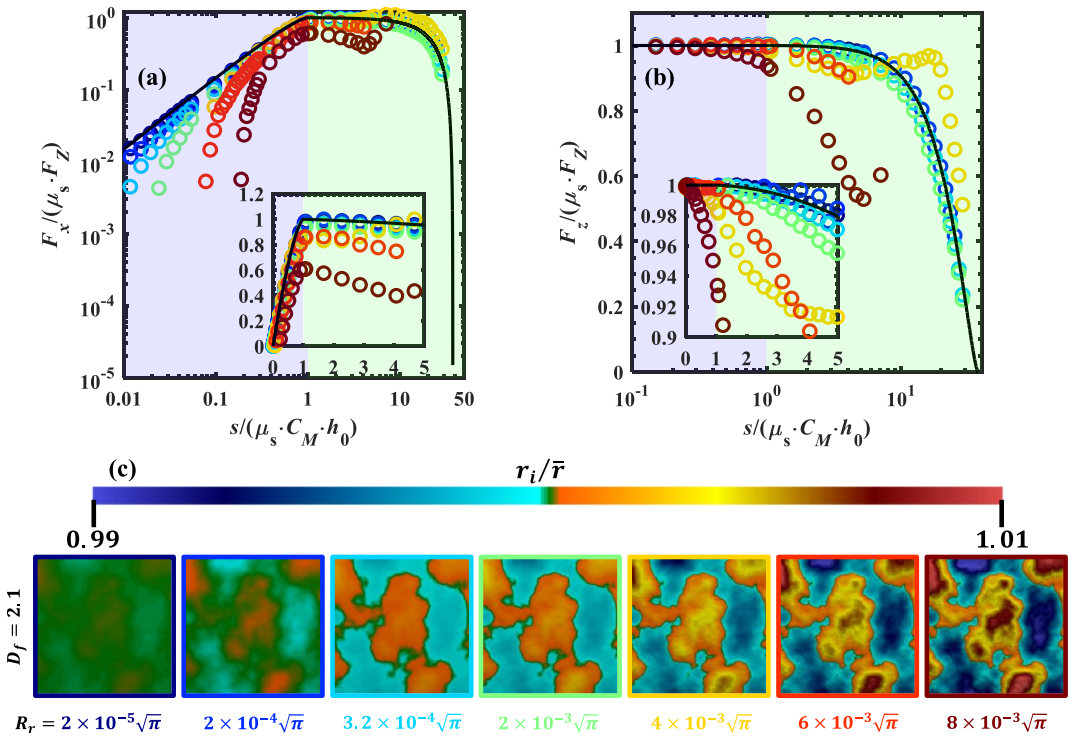

Figure 8. (a) Normalized traction forces, $\frac{F_x}{\mu_s F_Z}$, and normalized normal force, $\frac{F_z}{\mu_s F_Z}$ in (b), versus normalized transverse displacements, $\frac{s}{\mu_s C_M h_0}$, for rough elastic sphere contacts with various R_r (with the increase of R_r simulation parameters are listed in No. 2, 49, 4, and 53–56 in Appendix B), of which the top surface morphology in the mesh-fine zone is depicted in (c). Hot color means high R_r. Lines represent the extended Cattaneo-Mindlin solutions of smooth spheres, while circular points represent simulation results of rough sphere contacts.

necessity can be straightforwardly extended to studies of dynamic rupture propagation in earthquakes and other geophysical applications, where the explicit introduction of roughness in numerical methods such as Boundary Integral Method and FEM is desired, instead of directly incorporating experimentally derived laws, such as the rate and state dependent friction law. This is particularly relevant to simulations in Mollon et al. (2020), as the discrete fault gauge in such simulations is typically sandwiched by two rough surfaces.

In Figure 8 we show evolutions of F_x and F_z versus s across nearly three magnitudes of normalized root mean square roughness, R_r. At the first glance, with the increase of R_r, both normalized $F_x - s$ and $F_z - s$ curves gradually deviate from those of smooth sphere contacts. During the partial-sliding regime, $s \leq 1$, such departure of F_x encountered at the very beginning of tangential displacement is more evident than that of F_z, as indicated in Figure 8a. This is because directions of frictional forces tend to evolve from completely anisotropic (along the direction of macro tangential displacement, x) to nearly isotropic, and thus F_x decreases at the same s. Such a tendency of gradual deviation from the extended Cattaneo-Mindlin solution with higher R_r also occurs in Figure 8b for $F_z - s$ curves during the partial-sliding regime. It may seem perplexing that the frictional responses, as depicted by the normalized $F_x - s$ and $F_z - s$ curves for lower R_r are nearly identical to that of the smooth sphere contact. Roughness of small scales does indeed influence the frictional response, as illustrated by MD simulations in Luan and Robbins (2009, 2021). However, this study employs continuum scale computations, which can potentially break down at the specific length scales. The frictional response is controlled by the normal contact state. According to Greenwood and Tripp (1967), for the normal contact between two rough spheres the normal force and displacement curves would gradually converge to that of the Hertzian solution at the transition normal contact force (F_{tz}), that is, $F_{tz} \propto 2^{-\frac{1}{4}} R_r^{\frac{3}{2}} \bar{r}^2 \frac{E}{1-\nu^2}$, where E and ν are Young's modulus and Poisson's ratio, respectively. For cases of lower R_r, $h_0 = 0.01R > h_{t0}$, where h_{t0} is the normal contact interference at $F_z = F_{tz}$, the normal contact would converge to the Hertzian solutions for smooth sphere contact; as a result, the frictional response is manifested by the extended Cattaneo-Mindlin solution, as illustrated in Figure 8. With increasing R_r, obtained $F_z - s$ curves and $F_x - s$ curves would gradually deviate from the Hertzian solution, as shown in

Figure 8. This finding is consistent with Figure 6, indicating there is a competition mechanism between R_r and h_0 in determining the discrepancy of macro mechanical response with respect to that of smooth sphere contacts. It is noted that in Figure 8 for $R_r \geq 4 \times 10^{-3}\sqrt{\pi}$, both normalized $F_x - s$ and $F_z - s$ curves do not retain the shape of the extended Cattaneo-Mindlin solution at all; thus, the critical tangential displacement, δ_{su}, cannot be well predicted by $\mu_s C_M h_0$. Because of the high amplitude of randomness in morphology features, which brings sudden or unpredicted changes to both $F_x - s$ and $F_z - s$, a deterministic model to describe them is hard to be found. When and only when the normal contact interference is deep enough, representative results are accessible at the post-partial-sliding regime.

4.4. Influences of Wavelength Range

As indicated in Candela et al. (2012), fault surfaces exhibit multi-scaled morphology features across nine decades of length scales, which can be depicted by accumulative wavelengths. Since roughness is one of the important factors in determining frictional properties, it is necessary to discuss the influence of wavelength ranges approximating the surface topology on the contact. Instead of the nominally flat rough surfaces, we look at the contact of their asperities (deemed as rough sphere caps in this study), which are of more primary interest. Figure 9 illustrates influences of wavelength scope with the cut-off or shortest of $\lambda(2{,}000)$ and $R_r = 2 \times 10^{-5}\sqrt{\pi}$ or $2 \times 10^{-4}\sqrt{\pi}$ on macro contact response. Notably, for $n = 1$, SH has negligible effects on grain morphology (Mollon & Zhao, 2012), thus, when $\lambda_r(n) = \lambda(2)$ full-range wavelength is used to generate grain morphology. To achieve the representative results from the contact at mesh-fine zone, $R_r = 2 \times 10^{-5}\sqrt{\pi}$ and $2 \times 10^{-4}\sqrt{\pi}$ are selected, otherwise with much higher R_r the rough grain would not "roughly" retain the shape of the sphere. According to Zhao et al. (2017), $\lambda(8)$ is fine enough to represent the roundness scale of grain surfaces, below which is the roughness scale (Barrett, 1980). As depicted in Figure 9(e), with the increase of $\lambda_r(n)$ the macro asperity size gradually shrinks at the contact zone.

Globally at lower R_r, the extended Cattaneo-Mindlin solution can still well capture the evolutions of both $F_x - s$ and $F_z - s$ curves, as shown in Figures 9a and 9c; however, at higher R_r, δ_{su} in $F_x - s$ curves departs from $\mu_s C_M h_0$ when $\lambda_r(n) > \lambda(300)$. By contrast, the $F_z - s$ curves compare well with the extended Cattaneo-Mindlin solution at higher R_r. It is also noted, that is, in the insets of Figures 9c and 9d, that vibrations around analytical solutions are encountered in force-displacement curves due to the so-called cumulative partial-to-full sliding or repeated stick and slide state at single asperities; the vibration amplitudes, A, are dependent on both R_r and $\lambda_r(n)$, but such dependence is rather complicated and not monotonic. For $R_r = 2 \times 10^{-5}\sqrt{\pi}$, all curves of various $\lambda_r(n)$ show violent fluctuations except for the one of the median $\lambda_r(n) = \lambda(31)$ in the reference group, which is smooth (see the green curve in Figure 9c). In Figure 9d vibrations start to be encountered when the roll-off wavelength is shorter than $\lambda(15)$.

5. Discussions

Supported by the numerical modeling, here we elucidate that the critical tangential displacement of rough sphere contacts of various μ_s, h_0, and material properties can be well predicted by Cattaneo-Mindlin solution, as summarized in Figure 10a. Notably, simulated δ_{su} is determined by the average of displacements beyond which roughly continued drop occurs in both F_x and F_z. In Figure 10b, simulated δ_{su} influenced by R_r and $\lambda_r(n)$ of the same $\lambda_s(n) = \lambda(2{,}000)$ is summarized; $\delta_{su} = \mu_s \cdot C_M \cdot h_0$ still holds, except for some extreme cases. With the increase of R_r, simulated δ_{su} departs gradually from $\mu_s \cdot C_M \cdot h_0$. This is within anticipation, since it has been shown in Figure 8 the global shape of both $F_x - s$ and $F_z - s$ curves cannot be described by the extended Cattaneo-Mindlin solutions. Simultaneously, at higher R_r, simulated δ_{su} of cases with shorter roll-off wavelengths or narrower wavelength ranges also deviate from the analytical solution for smooth sphere contacts. Such a departure can be explained by the increased vibrations at contact interfaces due to the enlargement of macro asperity numbers, which can be seen in $F_z - s$ curves in the insets of Figure 9d and rough grain morphology in Figure 9e.

To elucidate the reason for the repeating well-performance of $\delta_{su} = \mu_s \cdot C_M \cdot h_0$ to predict the critical shear displacement for various rough sphere contacts, underlying revolutions of the contact interfaces can be tracked. Figure 11 provides the full evolution of the contact pressure p_N, traction along the projection of global x direction on the local contact plane q_x, traction along the y direction (perpendicular to the plane crossed by directions of p_N

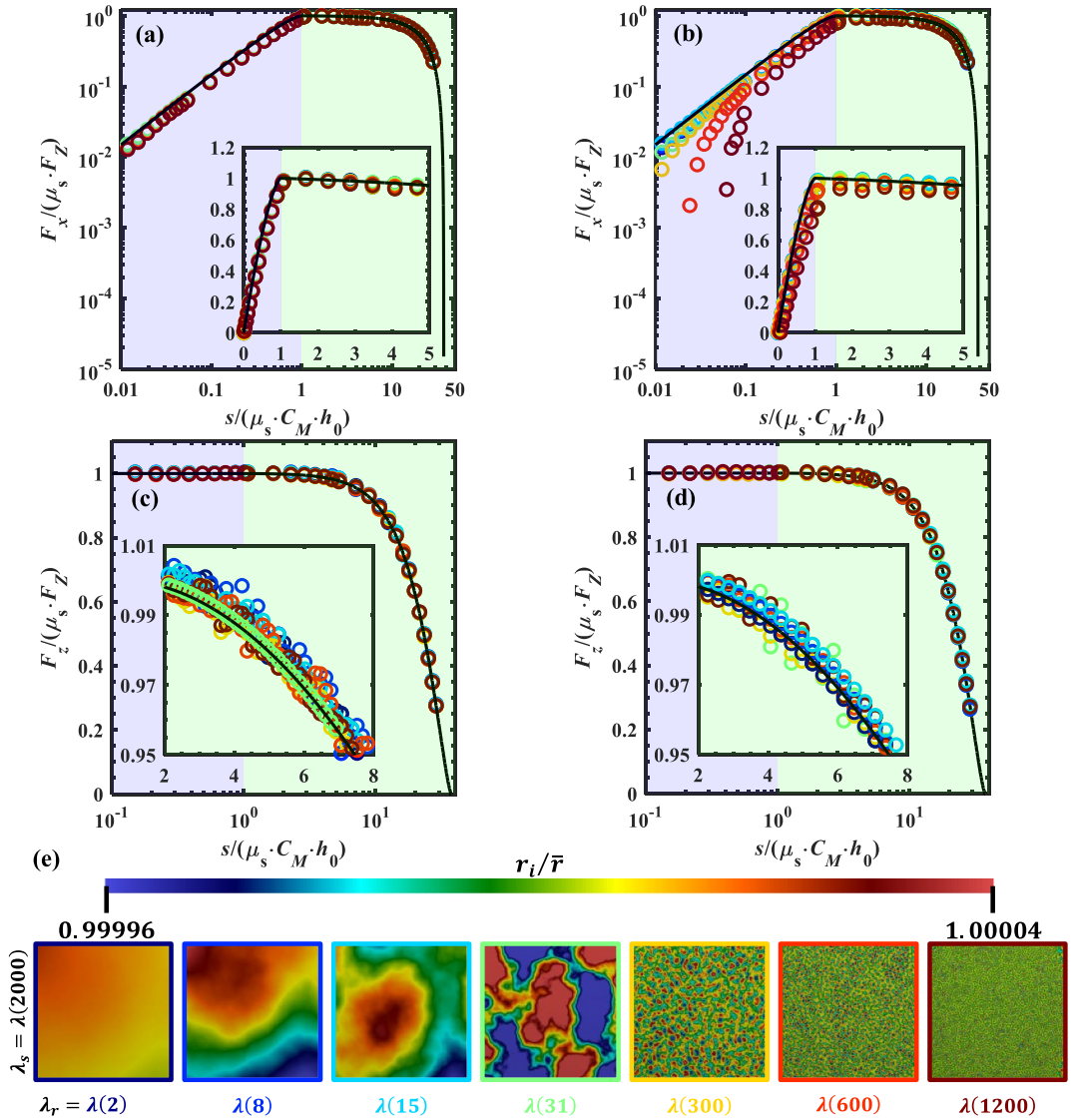

Figure 9. Normalized traction forces, $\frac{F_x}{\mu_s F_Z}$, in (a, b) and normalized normal force, $\frac{F_z}{\mu_s F_Z}$ in (c, d), versus normalized transverse displacements, $\frac{s}{\mu_s C_M h_0}$, for rough elastic sphere contacts with various roll-off wavelength, $\lambda_r(n)$. Panels (a) and (c) are for $R_r = 2 \times 10^{-5}\sqrt{\pi}$, while (b) and (d) are for $R_r = 2 \times 10^{-4}\sqrt{\pi}$. (e) The top surface morphology features in the mesh-fine zone for the group of $R_r = 2 \times 10^{-5}\sqrt{\pi}$. Notably, the morphology features of the group of $R_r = 2 \times 10^{-4}\sqrt{\pi}$ are the same as those of $R_r = 2 \times 10^{-5}\sqrt{\pi}$ except for the range of color map, of which it belongs to [0.9996, 1.0004], 10 times wider when compared with $R_r = 2 \times 10^{-5}\sqrt{\pi}$. Simulation parameters for the group of $R_r = 2 \times 10^{-5}\sqrt{\pi}$ are listed in No. 40–42, 2, and 43–45, while simulation parameters for the group of $R_r = 2 \times 10^{-4}\sqrt{\pi}$ are listed in No. 46–52. For the data point in (a)–(c) and the subfigure contour in (e), a hotter color indicates results extracted from the contact with a shorter roll-off wavelength. Lines represent analytical solutions of smooth sphere contact, while circular points represent simulation results of rough sphere contacts.

and q_y) on the contact plane q_y, and contacted node friction saturation $\hat{s}$, defined in Appendix C2. For purely elastic material, the contact pressure distributions of the similarly low R_r, yet distinct D_f, do not differ much from the smooth sphere. Compared with the realization of $(R_r, D_f) = (2 \times 10^{-5}\sqrt{\pi}, 2.1)$, the realization with higher D_f, yet the same R_r, only bring fluctuations on the distribution of p_N. The increased roughness results in a contact area very different from a disk, and at the same time, an irregular distribution of the contact pressure compared with that of the smooth sphere contact. The regions with higher contact pressure are not necessarily located closer to the central contact points, but widely distributed around the whole contact area and even at the boundary of it, as indicated in Figure 11a of

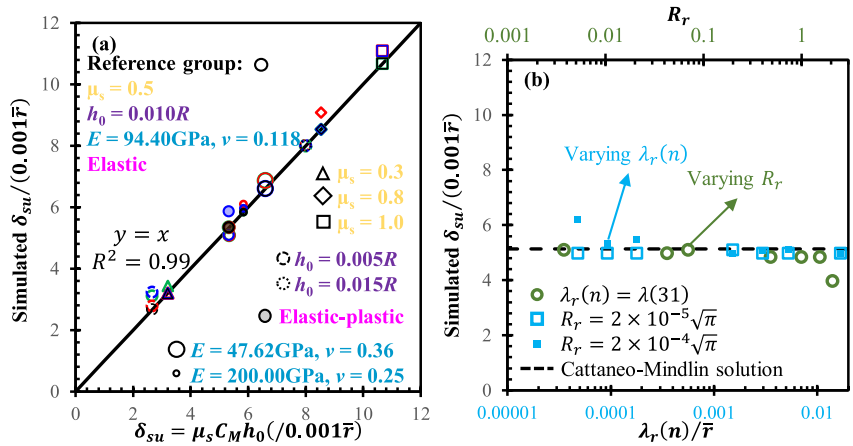

Figure 10. (a) Summary of simulated critical tangential displacement, δ_{su}, of rough sphere contacts influenced by micro friction coefficient, μ_s, normal contact displacement, h_0, and material properties; (b) Simulated δ_{su} versus relative roughness, R_r, and normalized roll-off wavelength, $\frac{\lambda_r(n)}{\bar{r}}$, for rough sphere contacts with the same fractal dimension (D_f), μ_s, h_0, cut-off wavelength ($\lambda_s(n) = \lambda(2{,}000)$), and elastic properties. In (a), color black, green, red, and blue represent $R_r = 0$, $(R_r, D_f) = (2 \times 10^{-5}\sqrt{\pi}, 2.1)$, $(R_r, D_f) = (2 \times 10^{-5}\sqrt{\pi}, 2.5)$, and $(R_r, D_f) = (32 \times 10^{-5}\sqrt{\pi}, 2.1)$, respectively.

$(R_r, D_f) = (2 \times 10^{-5}\sqrt{\pi}, 2.1)$. For elasto-plastic material, the pressure distribution is more homogeneous due to the plastic yielding at the contact interface. Another interesting observation is that for purely elastic material, the contact pressure does not really evolve in the whole partial-to-full sliding regime, while for elasto-plastic material, it is seen that the high contact pressure gradually disappears. This is because in the partial sliding regime, the in-plane tangential loading increases while the stress at the contact interface is bounded by its plasticity strength/yield surface. Therefore, the stress state has to evolve into another location at the yield surface where the shear stress is higher and the normal stress becomes smaller. Furthermore, a completely different pressure distribution in the full slide regime can be seen, indicating a different contact morphology/configuration and the necessity of no involvement in rough-flat simplification when considering rough sphere contacts.

The effect of the roughness is more pronounced (even for low R_r) for the in-plane shear traction, as shown in Figures 11b and 11c. When considering purely elastic material, for q_x we can see that at the small tangential loading there are contact points whose tractions are negative. These values gradually evolve and become positive at the transition to full slide. For q_y, tractions in both tangential directions exist even at the critical transition to full slide regime. However, its value is much smaller and equals about at most 5% of q_x. In full slide regime, these non-zero tractions are barely seen. For the in-plane traction, plasticity has played a significant role: for q_x, negative values are barely seen; for q_y, there are much fewer contact points with non-zero traction.

Figure 11d shows the evolution of the contacted node friction saturation: when the value $s = 1$, it means locally the contact point evolves into the full slide regime, otherwise it is in the state of the partial slide. It is seen that for purely elastic contact, with the increasing of the tangential loading, zones of contact points that have translated to the full slide state would not necessarily shrink toward the central contact point, especially for higher roughness. The distribution of the full-slide points is dependent on both contact morphology and loading conditions. While similar to the classical Cattaneo-Mindlin solution, the transition starts from the boundary of the contact interface toward the center for elasto-plastic contact, indicating that plasticity could alleviate the influences of roughness on friction evolution on the contact interface. Moreover, it is evident that local partial-slide exists even when the full slide regime of the contact interface sustains for a certain period. Such a paradoxical phenomenon, difficult to be seen in the contact between one rigid platen and a deformable rough sphere, is enhanced by roughness for more asperity interlockings, but relieved by plasticity for more flat contact interfaces due to the plasticity saturation. The contact nodes in the partial slide state initially distribute continuously or cluster, when the whole contact interface is in the partial slide regime; while upon entering the full slide regime, they distribute sporadically across the entire contact area. Such a transition process is called de-cluttering. In a short summary, at $s = \mu_s \cdot C_M \cdot h_0$ the vanishment of q_x independent of the global tangential displacement direction, x, the downscaling of the magnitude

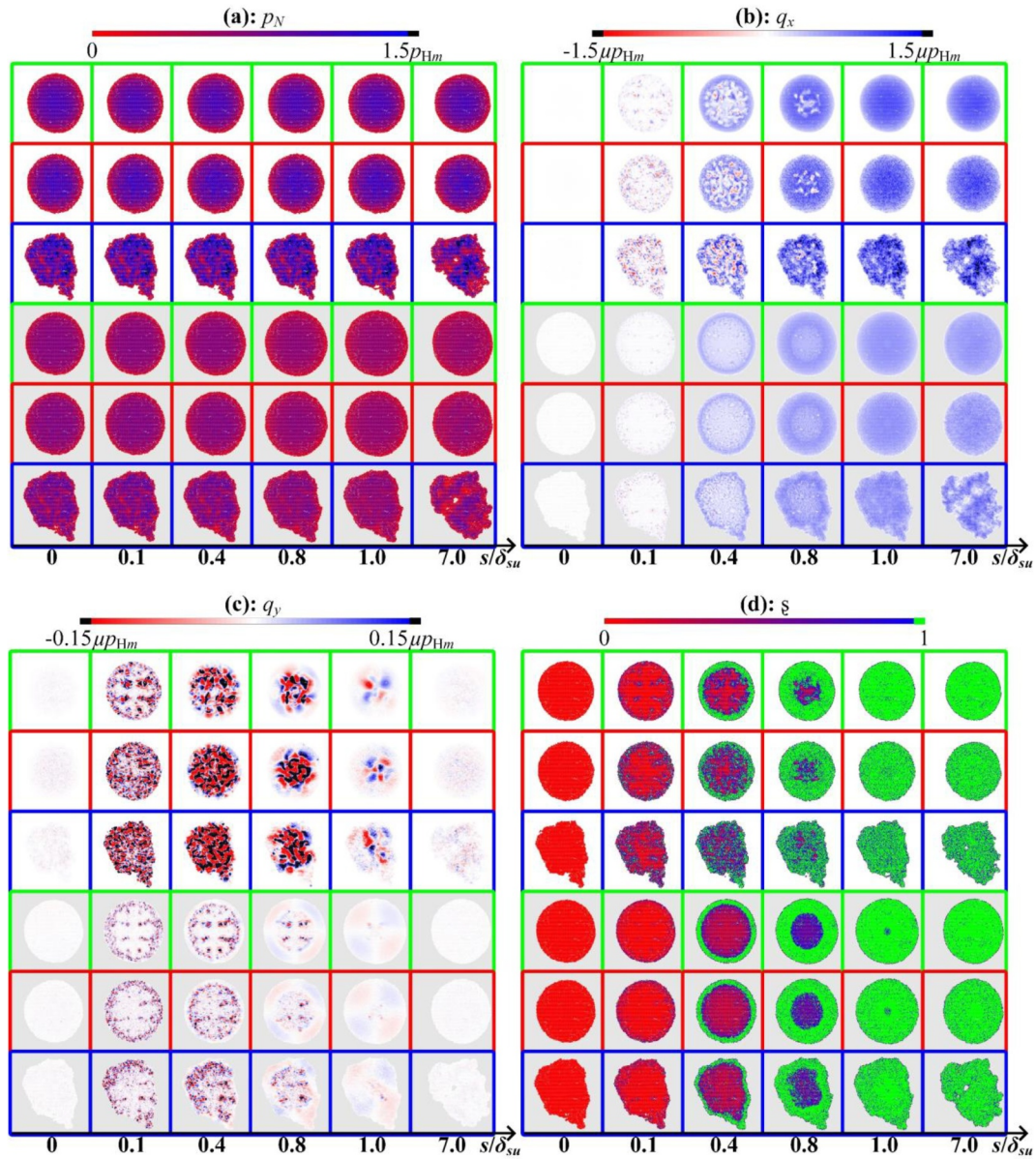

Figure 11. (a–d) The evolution of distributions of normal contact stress p_N, friction stress q_x and q_y, and friction saturation ş on contacted nodes with the normalized tangential displacement, $\frac{s}{\delta_{su}}$, for cases of elastic contacts featured by white background (No. 2–4 in Appendix B, the reference group) and elastic-plastic contacts featured by gray background (No. 26–28 in Appendix B, the elastic-plastic contact group). $p_{H,m}$ denotes the maximum normal contact stress of Hertzian sphere contact determined by Equation A5, with the same composite elastic modulus E^*, composite radius R^*, and normal contact distance h_0. Black zones in (a–c) are for nodes with $p_N > 1.5p_{H,m}$, $|q_x| > 1.5\mu_s p_{H,m}$, and $|q_y| > 0.15\mu_s p_{H,m}$, while green zones in (d) are for modes with ş = 1, of which the definition is defined in Appendix C2. Green, red, and blue contours of subfigures represent three typical morphology features $(R_r, D_f) = (2 \times 10^{-5}\sqrt{\pi}, 2.1)$, $(R_r, D_f) = (2 \times 10^{-5}\sqrt{\pi}, 2.5)$, and $(R_r, D_f) = (32 \times 10^{-5}\sqrt{\pi}, 2.1)$, respectively, of which the power spectrum and morphology features in the mesh-fine zone are provided in Figure 3.

of q_y, and the de-clustering of contacted nodes in partial-slide states explain the reason for the capacity of Cattaneo-Mindlin solution to predict the critical shear displacement of rough sphere contact.

The findings in this study have wide implications in geophysics. The most apparent application is DEM, which stands out as one of the most prevalent methods to simulate motions of discrete bodies in geophysics. In DEM, the

discrete bodies with their motions governed by Newton's second law, are usually considered as perfect circles in 2D and spheres in 3D. The discrete grains interact with each other via contact models with well-defined normal and frictional force-displacement relationships, such as the Hertzian-Mindlin model. In the frictional or tangential contact model, the tangential force would monotonically increase with the tangential displacement until reaching a peak at critical tangential displacement. Thus, this critical tangential displacement, denoted as δ_{su} in this study, is of significant importance to accurately compute friction force in DEM. Obtained force-displacement curves for tangential contact in this study and for normal contact in our previous study (Wei et al., 2020) can incorporate the influences of various morphological and material factors, such as relative roughness, fractal dimension, wavelength range, and plasticity. Although the morphology features generated by USH in this study are hard to import explicitly into the DEM geometry model, obtained force-displacement curves in this study can be directly mapped to the contact law of DEM to study the dynamics of rough spheres with target morphology features and material properties. Indeed, although the current DEM contact model has considered more fundamental Hertz-Mindlin solutions in normal and tangential directions, most of the simplified force-displacement curves (Chang et al., 1992; Jenkins & Strack, 1993) are thermodynamically inconsistent due to the omitted load history. To bridge this gap, Elata and Berryman (1996) added a residual tangential displacement (when the tangential contact force is unloaded while keeping the normal contact displacement fixed) to Equation A8 to substitute the detailed account of the load history. Since the residual displacement is no more than δ_{su}, which is also in Equation A8, our quantitative findings about δ_{su} influenced by various geometrical and loading factors can be imported to the improved tangential forces model in DEM.

Another obvious implication is wave propagation in granular materials, such as seismic compression (*P*-) and shear (*S*-) waves, which has been extensively studied and demonstrates complex phenomena and rich features: power-law velocity scaling, dispersion, and attenuation (Aki, 1980; Jia et al., 1999; Kjartansson, 1979). However, the precise role of inter-grain behavior highly correlated to grain morphology on these features remains a continued research interest. Generally, grain morphology can be separately depicted in two length scales: the global shape and the fine-scale roughness. In recent experiments reported by Yang and his collaborators (Liu & Yang, 2018), the void-ratio-function normalized shear wave velocity in the packing of rough and angular Fujian sands is nearly twice that of smooth and rounded Ottawa sands under the same confining pressure and of similar global grain shapes quantified by elongation, sphericity, and convexity indices. Interestingly, in another numerical study about superellipsoid-based DEM simulations featuring aspherical Hertzian contact laws by Yang and his collaborators (Tang & Yang, 2021), it was found wave transmits in superellipsoid-shaped grains of the same elongation but different angularity by nearly the same speed. The conclusion, wherein shear wave velocity can be only slightly influenced by grain elongation for packings with angular grains, is contrary to their experimental observations. The intriguing inconsistency between their numerical and experimental results that higher wave velocity can be found in rough grain packing can be explained by our results in this study. Their numerical simulations are just for smoothed grains without considering roughness; in our results retaining the same globally spherical shape but various roughness it is clear that in Figure 8 shear stiffness, k_s, between grains increases evidently for rougher spheres. According to Winkler (1983), shear wave velocity, V_s, can be explicitly determined by normal contact stiffness, k_n, and k_s between grains: $V_s = \sqrt{f(k_n + 1.5k_s)/\rho}$, where V_s is the shear wave velocity, ρ is the grain density, and f is a function of grain coordinate number, porosity, and grain size. Under dense packing, the grain normal contact force is plausibly assumed to be as high as the critical value to converge to Hertzian solution; the increase of V_s in experiments of Liu and Yang (2018) can be explained by the increasing of k_s. The capability of large grain contact shear stiffness to enhance the wave propagation speed in uncemented granular sediments has also been reported in our previous study (Zhai et al., 2020).

The present study also provides an intuitive numerical framework at desired resolutions, providing insights into analyzing the earthquake occurrence on the asperity basis, such as the asperity model (Lay & Kanamori, 1981), whereas large earthquake rupture zones usually occur over discrete, non-overlapping segments of the convergent zone and these segments with strong slide resistance are called asperities. Currently, the shear stress distribution in Mindlin solution has been widely applied to deriving the in-plane and anti-plane mode stress intensity factor in the elliptical crack problem for shear-induced rupture (Das & Kostrov, 1983, 1985; Gao, 1989). Since the asperity contact area is not modestly, but significantly different from a circle, our anisotropic frictional stress distribution in Figures 10b and 10c could provide a more fundamental solution to shear-induced rupture; furthermore, our results in the full slide zone are beneficial to dynamic earthquakes, while the original Cattaneo-Mindlin solution is

just for the partial-to-full slide regime, where the contact area is "static." This study highlights the influence of roughness parameters in producing local slides and evolving stress distributions, which are found to be distinct across contacts. In Figure 10d the recurrence of partial or full slide state can be seen at some contact zones, especially for contacts of higher roughness. The strong correlation between local slide patterns and surficial roughness agrees with the numerical studies (Allam et al., 2019), geodetic studies (Milliner et al., 2015), and paleoseismic studies (Rockwell et al., 2015). However, this study only furnishes a simplified pathway, motivating the development of future models for fault triggering incorporating aspects of moisture effects and complex loading and boundary conditions.

Although our studies are conducted using numerical simulations, existing experimental tools widely implemented in geophysical research are readily accessible to validate the extracted findings. These experimental validations can be realized in two folds: macroscopic contact responses under different roughness conditions and microscopic contacts and their spatiotemporal evolutions. At first, the rough spheres with well-controlled micro morphology features can be generated using 3D printing (Wei et al., 2021) and then adopted similar experimental set-ups for frictional contact between two grains (Kasyap et al., 2021; Sandeep et al., 2019). In addition to macro contact responses, characterized by force-displacement relations, micro-level information such as contact and frictional stresses can be tentatively measured for certain resolution and accuracy, using micro-electromechanical systems (Scheibert et al., 2009). Since the quasi-static loading is adopted in this study, fast X-ray computed tomography (Zhai et al., 2020) can be employed to track the 3D spatial evolutions of asperity contact between two non-transparent rough surfaces, which is helpful in understanding the friction saturation.

6. Conclusions

In this paper, we focus on frictional behavior between two rough spheres. After extending and validating the Cattaneo-Mindlin problem for smooth sphere contacts to incorporate the full slide regime, we carried out intensive and systematic FEM simulations, for the first time, for frictional contact between two isotropic rough spheres generated based on ultra-high degree SH. Gigantic parameter studies are conducted to reveal the ramifications of rough sphere contacts due to the micro friction coefficient, normal contact interference, material property, relative roughness, fractal dimension, and wavelength range. The micromechanics for the observed transition between the partial to full sliding modes are also revealed by investigating the evolution of the spatial distribution of micro contacts, as well as their contact pressure and local slides. In summary, the main conclusions of this study are:

- The proposed extended Cattaneo-Mindlin solution for smooth sphere contacts can approximately describe macro contact responses (macro normal- and friction-force-displacement curves) between two rough sphere contacts under various material properties, micro friction coefficients, normal contact interferences; $\delta_{su} = \mu_s \cdot C_M \cdot h_0$ in the Cattaneo-Mindlin solution can well predict the critical tangential displacement. However, under some extreme cases, that is, extremely high relative roughness and narrow wavelength, the shape of macro force-displacement curves departs the analytical solution much.
- Existing roughness would make the force-displacement curves slightly depart from those of smoothed sphere contacts. Meanwhile, such an impact can be enhanced with the increase of roughness, but weakened by material plasticity.
- With the input roughness parameters from the range of real granular materials, it is found that the rough sphere contact response is more sensitive to the changes in relative roughness than the fractal dimension.

Appendix A: A Short Review of Cattaneo and Mindlin Problem

The partial-to-complete slide motion between two spheres with the radius of R is defined as follows. The original center of X-Z coordinate system is at the mass center of the lower sphere, (x_l, z_l), $= (0, 0)$. The center of the upper sphere is given as (x_u, z_u). During the whole transverse motion, the lower sphere is fixed and restricted to any rotations, which is similar to the relevant experimental study (Cole et al., 2010). After being vertically compressed of a displacement h_0, the upper sphere is subjected to a pure horizontal displacement along the x-axis, that is, it is constrained as $z_u = Z_h$, where Z_h is the vertical distance between centers of the two identical spheres. For the normal contact regime shown in the left inserted schematic in Figure 1, the

normal contact force, N, between the two contacted spheres is a function of the overlap, h, according to the Hertzian contact model (Johnson, 1985),

$$N = \frac{4}{3}E^* \cdot R^{*\frac{1}{2}} \cdot h^{\frac{3}{2}}, \tag{A1}$$

where E^* and R^*, denoting the effective elastic modulus and radius, are defined as

$$\frac{1}{E^*} = \frac{1-{v_1}^2}{E_1} + \frac{1-{v_2}^2}{E_2}, \tag{A2}$$

and

$$\frac{1}{R^*} = \frac{1}{R_1} + \frac{1}{R_2}, \tag{A3}$$

with E_1 and E_2 Young's modulus, v_1 and v_2 Poisson's ratio, R_1 and R_2 radius, of the contacted spheres. Under the normal contact force, a circular contact area of radius a forms. The normal contact stress (p_N) on any contact point depends on its radial distance to the contact center (r):

$$p_N(r) = p_{N,\,m} \cdot \left[1 - \left(\frac{r}{a}\right)^2\right]^{\frac{1}{2}}, \tag{A4}$$

where $p_{N,m} = p_N(r=0)$ is the maximum normal contact stress, located in the contact center. By integrating $p_N(r)$ over the circular contact area, $p_{N,m}$ can be explicitly determined as

$$p_{N,\,m} = \frac{3N}{2\pi a^2} = \frac{3}{2} \cdot \frac{N}{S_A}, \tag{A5}$$

where $S_A = \pi a^2$ is the contact area. The contact radius, a, is also directly related to h and R^* (Johnson, 1985),

$$a = \sqrt{R^* \cdot h}, \tag{A6}$$

Substituting Equations A1 and A6 to Equation A5, the maximum normal contact stress reads

$$p_{N,\,m} = \frac{2E^* h^{\frac{1}{2}}}{\pi R^{*\frac{1}{2}}}. \tag{A7}$$

For a similar situation in the middle-inserted schematic of Figure 1, Cattaneo (1938) and Mindlin (1949) derived the relation between the traction force, $F_x(s)$ and the tangential displacement, s, under a constant normal force, $F_z(s)$,

$$F_x(s) = \underbrace{\frac{4}{3}E^* R^{*\frac{1}{2}} h_0^{\frac{3}{2}}}_{N} \mu_s \left[1 - \left(1 - \frac{s}{\delta_{su}}\right)^{\frac{3}{2}}\right],\ s \le \delta_{su}, \tag{A8}$$

where μ_s is the set dry Coulomb friction coefficient, s is the slide displacement, δ_{su} is the ultimate tangential slide displacement when sliding happens. In this relation, the following assumptions were made: (a) $p_N(r)$ follows the distribution of Hertzian contact model, (b) $p_N(r)$ and the tangential stress, $q_T(r)$, can be treated separately, and (c) $q_T(r=a)$ will go infinity for the complete stick situation. During the partial-to-full slide transition, $q_T(r)$ obeys the following equation,

$$q_T(r) = \begin{cases} \dfrac{3\mu_s \cdot N}{2\pi \cdot {r_{sp}}^3} \cdot \sqrt{{r_{sp}}^2 - r^2}, & r_{sk} < r \le r_{sp} \\ \dfrac{3\mu_s \cdot N}{2\pi \cdot {r_{sp}}^3} \cdot \left(\sqrt{{r_{sp}}^2 - r^2} - \sqrt{{r_{sk}}^2 - r^2}\right), & r \le r_{sk} \end{cases}, \tag{A9}$$

as indicated in Figure 1b, $r_{sk} = c$ denotes the radius of the continuously shrinking stick zone, and $r_{sp} = a$ is the outer radius of the annulus slide area. The relation between the two reads as

$$\frac{c}{a} = \left(1 - \frac{F_x}{\mu_s F_z}\right)^{\frac{1}{3}}, \tag{A10}$$

However, in this study we consider a constant normal contact separation, h_0, rather than a constant $F_z(s)$ for the tangential contacts. Akin to Equation A8, under varying $F_z(s)$ the relation between $F_x(s)$ and s_p is solved by Mindlin and Deresiewicz (1953). According to Mindlin and Deresiewicz (1953), if "simple loading history," during which the variation rate of shear force ($F_x(s)$) is higher than the product of μ_s and normal force ($F_z(s)$),

$$\left|\frac{dF_x(s)}{dt}\right| \ge \mu_s \left|\frac{dF_z(s)}{dt}\right| \text{ or } |\Delta F_x(s)| \ge \mu_s \cdot |\Delta F_z(s)|, \tag{A11}$$

is conformed to, after each increment of $F_x(s)$ and $F_z(s)$, normal contact pressure ($q_N(r)$) follows the distribution in classical solutions for the partial-slide regime derived from frictional sphere contact under constant normal forces. Due to the existence of the stick zone, the contact center is fixed in the partial-slide regime, thus, $h = h_0$ always holds in this regime for constant $F_z(s)$. As a result, $|\Delta F_z(s)| = 0$. Meanwhile, the traction gradually increases, that is, $|\Delta F_x(s)| > 0$. Accordingly, Equation A11 is met in our boundary conditions, thus solutions of traditional Cattaneo and Mindlin problem suit our boundary conditions of the partial-slide regime, schematically shown in Figure 1.

Appendix B: Simulation Parameters of All Cases

See Tables B1 and B2.

Table B1
Simulation Details of Cases From No. 1 to 39 With $\lambda_r = \lambda(31)$

No.	μ_s	Material properties	R_r	D_f	$h_0(R)$
1	0.5	①	0		0.010
2	0.5	①	$2 \times 10^{-5}\sqrt{\pi}$	2.1	0.010
3	0.5	①	$2 \times 10^{-5}\sqrt{\pi}$	2.5	0.010
4	0.5	①	$32 \times 10^{-5}\sqrt{\pi}$	2.1	0.010
5	0.3	①	0		0.010
6	0.3	①	$2 \times 10^{-5}\sqrt{\pi}$	2.1	0.010
7	0.3	①	$2 \times 10^{-5}\sqrt{\pi}$	2.5	0.010
8	0.3	①	$32 \times 10^{-5}\sqrt{\pi}$	2.1	0.010
9	0.8	①	0		0.010
10	0.8	①	$2 \times 10^{-5}\sqrt{\pi}$	2.1	0.010
11	0.8	①	$2 \times 10^{-5}\sqrt{\pi}$	2.5	0.010
12	0.8	①	$32 \times 10^{-5}\sqrt{\pi}$	2.1	0.010
13	1.0	①	0		0.010
14	1.0	①	$2 \times 10^{-5}\sqrt{\pi}$	2.1	0.010
15	1.0	①	$2 \times 10^{-5}\sqrt{\pi}$	2.5	0.010
16	1.0	①	$32 \times 10^{-5}\sqrt{\pi}$	2.1	0.010

Table B1
Continued

No.	μ_s	Material properties	R_r	D_f	$h_0(R)$
17	0.5	②	0		0.010
18	0.5	②	$2 \times 10^{-5}\sqrt{\pi}$	2.1	0.010
19	0.5	②	$2 \times 10^{-5}\sqrt{\pi}$	2.5	0.010
20	0.5	②	$32 \times 10^{-5}\sqrt{\pi}$	2.1	0.010
21	0.5	③	0		0.010
22	0.5	③	$2 \times 10^{-5}\sqrt{\pi}$	2.1	0.010
23	0.5	③	$2 \times 10^{-5}\sqrt{\pi}$	2.5	0.010
24	0.5	③	$32 \times 10^{-5}\sqrt{\pi}$	2.1	0.010
25	0.5	④	0		0.010
26	0.5	④	$2 \times 10^{-5}\sqrt{\pi}$	2.1	0.010
27	0.5	④	$2 \times 10^{-5}\sqrt{\pi}$	2.5	0.010
28	0.5	④	$32 \times 10^{-5}\sqrt{\pi}$	2.1	0.010
29	0.5	①	0		0.005
30	0.5	①	$2 \times 10^{-5}\sqrt{\pi}$	2.1	0.005
31	0.5	①	$2 \times 10^{-5}\sqrt{\pi}$	2.5	0.005
32	0.5	①	$32 \times 10^{-5}\sqrt{\pi}$	2.1	0.005
33	0.5	①	0		0.015
34	0.5	①	$2 \times 10^{-5}\sqrt{\pi}$	2.1	0.015
35	0.5	①	$2 \times 10^{-5}\sqrt{\pi}$	2.5	0.015
36	0.5	①	$32 \times 10^{-5}\sqrt{\pi}$	2.1	0.015
37–39	0.5	①	$32 \times 10^{-5}\sqrt{\pi}$	2.1	0.010

Note. (i) Parameters in red are for the reference group of simulations; (ii) Colorful backgrounds of parameters indicate differences from the reference group.

Table B2
Simulation Details of Cases From No. 40 to 55 With Materials Properties of ①, $\mu_s = 0.5$, $h_0(R) = 0.010$, and $D_f = 2.1$

No.	R_r	$\lambda_r(n)$
40	$2 \times 10^{-5}\sqrt{\pi}$	$\lambda(2)$
41	$2 \times 10^{-5}\sqrt{\pi}$	$\lambda(8)$
42	$2 \times 10^{-5}\sqrt{\pi}$	$\lambda(15)$
43	$2 \times 10^{-5}\sqrt{\pi}$	$\lambda(300)$
44	$2 \times 10^{-5}\sqrt{\pi}$	$\lambda(600)$
45	$2 \times 10^{-5}\sqrt{\pi}$	$\lambda(1,200)$
46	$2 \times 10^{-4}\sqrt{\pi}$	$\lambda(2)$
47	$2 \times 10^{-4}\sqrt{\pi}$	$\lambda(8)$
48	$2 \times 10^{-4}\sqrt{\pi}$	$\lambda(15)$
49	$2 \times 10^{-4}\sqrt{\pi}$	$\lambda(31)$
50	$2 \times 10^{-4}\sqrt{\pi}$	$\lambda(300)$
51	$2 \times 10^{-4}\sqrt{\pi}$	$\lambda(600)$
52	$2 \times 10^{-4}\sqrt{\pi}$	$\lambda(1,200)$
53	$2 \times 10^{-3}\sqrt{\pi}$	$\lambda(31)$
54	$4 \times 10^{-3}\sqrt{\pi}$	$\lambda(31)$
55	$6 \times 10^{-3}\sqrt{\pi}$	$\lambda(31)$
56	$8 \times 10^{-3}\sqrt{\pi}$	$\lambda(31)$

Appendix C: Details and Validations of FEM Simulations

FEM simulations were conducted in the commercial finite element (FE) package, ABAQUS (2016). Full integration for an element, the total mass of which is defined by a lumped mass matrix and averagely distributed over its four nodes, is considered for virtual work. Since the implicit approach is too memory intensive and even not possible for significant nonlinearity of contacts between rough surfaces, the explicit schematic is usually employed. Within the augmented Lagrangian framework, FE discretization leads to a discrete system of equations,

$$\mathbf{M} \cdot \ddot{\mathbf{u}} + \mathbf{F_i} - \mathbf{F}_e = \mathbf{0}, \tag{C1}$$

where $\ddot{\mathbf{u}}$ is the acceleration vector, $\mathbf{M}$ the diagonal mass matrix, and $\mathbf{F}_i$ and $\mathbf{F}_e$ the internal and external force arrays. This equation is discretized in time by the central difference integration framework:

$$\dot{\mathbf{u}}_{n+1/2} = \dot{\mathbf{u}}_{n-1/2} + \frac{\Delta t_{n+1} + \Delta t_n}{2} \ddot{\mathbf{u}}_n, \tag{C2}$$

$$\mathbf{u}_{n+1} = \mathbf{u}_n + \Delta t_{n+1} \dot{\mathbf{u}}_{n+1/2}, \tag{C3}$$

$$\Delta t = \sqrt{\frac{\rho}{E}} \ell, \tag{C4}$$

where n is the nth time step or increment, u a degree of freedom, Δt the length of stabilized time step, ρ the bulk material density, and E the elastic modulus. Mass scaling of ρ is permitted for the elements, of which their Δt is shorter than a constant target length. Although the explicit schematic and mass scaling are utilized, it has been checked that the kinetic energy never takes up more than 1% of internal energy during the sliding process (see Figure C3), indicating that our simulation is deemed to be quasi-static.

We conduct the mesh size sensitivity study for the fine mesh zone with the mesh size, ℓ, using the contact between an elastic sphere, of $E = 94.4$ GPa and $\nu = 0$, and a rigid flat platen. As demonstrated in Figure C1, the results of $\ell = 1.5 \times 10^{-3}R$ and its half, $\ell = 7.5 \times 10^{-4}R$, coincide with each other. Meanwhile, the normal contact force from the linear element, with four integration points and the tetrahedral shape, is slightly higher than that from the quadratic element, with the same shape but 10 integration points. For FEM simulations, the results in Figure C1 are self-consistent, as the quadratic elements are softer and more capable to deform due to their shape function. As a result, when using the same contact algorithm, the macro normal contact force of quadratic elements is lower than the linear elements. Considering the computational efficiency and better approximation of the Hertzian solution, linear elements are applied to carry out FEM simulations, as have been commonly adopted by many other relevant studies (Hyun et al., 2004; Lengiewicz et al., 2020; Pei et al., 2005; Zhang et al., 2019).

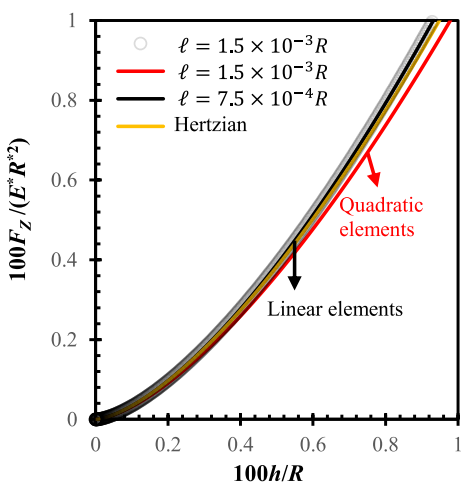

Figure C1. Comparisons of normal contact response (normalized normal contact force vs. normalized normal contact displacement) for the contact between an elastic sphere and a rigid planar surface between finite element method results of different mesh sizes and element types, referenced with the Hertzian contact solution.

In our simulations, a linear bulk viscosity damping model was employed to damp elements with the highest frequencies. This was used to prevent the FEM simulation from failing because of the high ratio (e.g., >1) of the deformation rate to wave speed at elements. The damping model generates a bulk viscosity pressure (p_l) linear to the element volumetric strain rate ($\dot{\varepsilon_v}$),

$$p_l = b\rho c_d L_e \dot{\varepsilon_v}, \tag{C5}$$

where $b = 0.06$ is the damping parameter, $\rho = 2.65 \times 10^3$ kg/m^3 the material density, c_d the current dilatational wave speed, and L_e the element characteristic length. As shown in Figure C2a of the response letter using the case No. 4, in Appendix C to calibrate rate and damping parameters, negligible differences can be observed across obtained results for simulations with different values of damping. Upon the completion of normal compression, the normal velocity has decreased to zero at the 1,000,000th timestep, and the

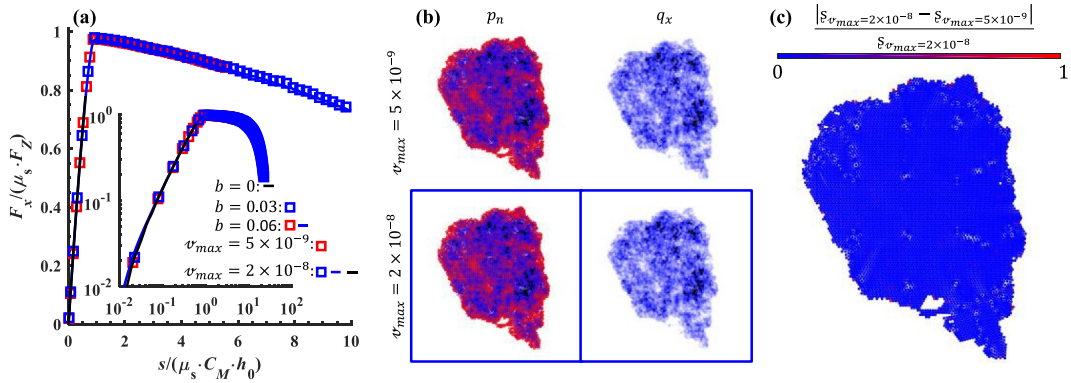

Figure C2. Convergence studies of applied normalized maximum velocity (υ_{max}) by $\frac{R}{\Delta t}$ and linear damping parameter, where Δt means the length of constant timestep; (b) Comparison of the distributions of p_n and q_x at $s/(\mu_s \cdot C_M \cdot h_0) = 1$ between different υ_{max}; and (c) Error in local partial-slide denoted by friction saturation induced by different υ_{max}.

ratio of kinetic energy to internal energy is only about 10^{-7}, as shown in Figure C3. This static state for both spheres was sustained for another 100,000 timesteps to better damp the kinetic energy and elastic waves. The energy ratio was less than 5×10^{-8} via this manifestation just before the start of tangential motion. Figure C2a also indicates that the convergency of the macro $F_x - s$ curve has been achieved for the tangential velocity applied in this study. We further confirm in Figures C2b and 1c that our numerical results in local partial-slide have negligible rate dependence for the maximum speed applied in this study.

C1. Material Properties

Rough spheres are assigned material constitutive models associating isotropic linear elasticity with or without Mises plasticity. The plasticity is represented as a typical isotropic power-law strain hardening:

$$\overline{\sigma} = \sigma_Y + \acute{k} \cdot (\varepsilon_p)^{\eta}, \tag{C6}$$

where $\overline{\sigma} = \sqrt{3S_{ij}S_{ij}/2}$ is the current Mises yield stress, S_{ij} the deviatoric stress tensor, $\varepsilon_p = \sqrt{2E^p_{ij}E^p_{ij}/3}$ the equivalent plastic strain, E^p_{ij} the deviatoric plastic strain tensor, σ_Y the initial yield stress, and $\acute{k}$ and η hardening parameters. The isotropic linear elasticity is only featured with two parameters: the Young's modulus (E) and Poisson's ratio (v). All the material parameters used in simulations are summarized in Table C1, where (E, v) = (47.62 GPa, 0.360) is for sandstone, (E, v) = (94.40 GPa, 0.118) for silica sand, and (E, v) = (200.00 GPa, 0.250) for steel.

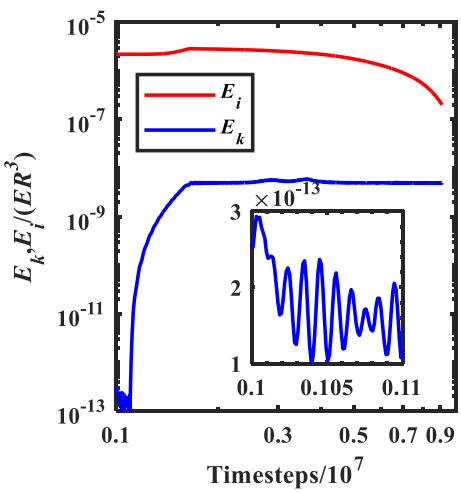

Figure C3. Energy evolution after completion of the pure normal compression process. E_i and E_k are internal and kinetic energies, respectively.

C2. Contact and Friction Model

Contact behavior is simulated by the balanced master-slave contact pair (ABAQUS, 2016) formed by two mesh-based surfaces. We have confirmed that all contacts occur in the fine-mesh zone. Compared with the pure master-slave contact pair, such a contact pair with the kinematic contact algorithm and enforcement of contact conditions can decrease illness induced by large penetrations between contacted surfaces. The contact formulation is categorized into normal and frictional contacts, both of which are based on finite sliding formulation, enabling any arbitrary motions between two contacted surfaces. For contacted nodes, we adopt the standard Coulomb friction model where no relative motion occurs if the equivalent frictional stress,

$$q_e = \sqrt{{q_x}^2 + {q_y}^2}, \tag{C7}$$

Table C1
Material Properties Used in Finite Element Methods Simulations

No.	E (GPa)	v	σ_Y (MPa)	κ (MPa)	η
①	94.40	0.118			
②	47.62	0.360			
③	200.00	0.250			
④	94.40	0.118	478.66	4,681.02	0.3

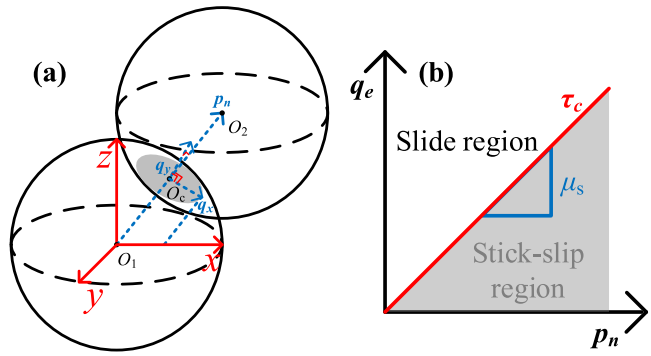

Figure C4. (a) Definitions of the local contact directions on or perpendicular to the contact plane; (b) The definition of the dry Coulomb friction model.

on the contact plane shown in Figure C4a is smaller than the critical frictional stress,

$$\tau_c = \mu_s \cdot p_n, \tag{C8}$$

as shown in Figure C4b, where p_n is the normal contact pressure, and μ_s the set friction coefficient. Notably, q_x is frictional stress on the projection of the global x axis on the contact plane, while q_y is the frictional stress on the contact plane and perpendicular to the surface crossed by p_n and q_x. Contacted node friction saturation (ş) is also defined as the ratio of concurrently computed friction coefficient ($\mu_ç$) to given dry Coulomb friction coefficient (μ_s),

$$ş = \frac{\mu_ç}{\mu_s}, \tag{C9}$$

where $\mu_ç = q_e/p_n$.

Appendix D: Relevant Definitions and Details of Ultra-High Degree SH

In a spherical coordinate system, surficial points of a star-shaped grain can be approximated using the SH function, $Y_n^m(\theta, \varphi)$, via denoting its radial length,

$$r(\theta, \varphi) = \sum_{n=0}^{\infty} \sum_{m=-n}^{n} c_n^m Y_n^m(\theta, \varphi), \tag{D1}$$

where $\theta \in [0, \pi]$ and $\varphi \in (0, 2\pi]$ are the latitudinal and longitudinal coordinates respectively, and c_n^m are the SH coefficients of degree n and order m. n is sometimes called spherical wavenumber. With the help of Parseval's theorem, the PS, L_n, at each SH frequency can be measured by

$$L_n = \left\| f_n \right\| = \sqrt{\sum_{m=-n}^{n} \left\| c_n^m \right\|^2}, \tag{D2}$$

where $\|\cdot\|$ is the L_2 norm. Some definitions associated with the mean roughness to quantify how rough grain surface is different from its mean radial length are necessary. The average radius length, $\overline{r}$, equals its c_0-determined sphere, R_0, reads as

$$\overline{r} \cong R_0 = c_0 \cdot Y_0(\theta, \varphi). \tag{D3}$$

where $Y_0(\theta, \varphi) = \frac{1}{2\sqrt{\pi}}$. In this study, we generate unit spheres, thus $c_0 = 2\sqrt{\pi}$. Parseval's theorem enables direct calculation of the mean squared distance (M_{sd}) between two grains only using their c_n^m without approximate sampling, such as the geodesic structure from an iterative icosahedron subdivision of spherical (θ,φ) space. In addition, a correction is needed, since $\int_0^{2\pi}\int_0^{\pi} Y_n^m(\theta, \varphi) \cdot \left[Y_n^m(\theta, \varphi)\right]^* \cdot \sin\theta \, d\theta d\varphi = 4\pi \neq 1$. With $c_{1,\,n}^m$ and $c_{2,\,n}^m$ denoting SH coefficients of two grains, M_{sd} reads as $\frac{1}{4\pi}\sum_{n=0}^{\infty}\sum_{m=-n}^{n}\|c_{1,\,n}^m - c_{2,\,n}^m\|^2$. If we set $c_{1,\,n}^m = c_n^m$ and $c_{2,\,n}^m = c_0^0$,

$$M_{sd} = \frac{1}{4\pi}\sum_{n=1}^{\infty}\sum_{m=-n}^{n}\left\| c_n^m \right\|^2. \tag{D4}$$

Simultaneously, for quantifying the roughness of half space or closed surface, the concept related to discrete approximation, mean square roughness (M_{sr}) or its square root (S_q), is more frequently mentioned,

$$M_{sr} = {S_q}^2 = \frac{1}{l}\sum_{l=1}^{l}(R_l - R_0)^2, \tag{D5}$$

where l is the number of detached surficial points. When l is large enough, we arrive at

$${S_q}^2 = M_{sd} = \frac{1}{4\pi}\sum_{n=1}^{\infty}\sum_{m=-n}^{n}\left\| c_n^m \right\|^2. \tag{D6}$$

Next, we will introduce how randomness is created in surface generation in ultra-high SH. If we apply the cut-off wavelength at $n = 2{,}001$, SH coefficients c_n in Equation D1 can be explicitly denoted:

$$c_n = \begin{pmatrix} c_0 \\ c_1 \\ c_2 \\ \vdots \\ c_{30} \\ c_{31} \\ \vdots \\ c_{2,\,000} \end{pmatrix}^T = \left(\begin{array}{c} 2\sqrt{\pi} \\ \begin{pmatrix} c_1^{-1} & c_1^0 & c_1^1 \end{pmatrix}^T \\ \begin{pmatrix} c_2^{-2} & c_2^{-1} & c_2^0 & c_2^1 & c_2^2 \end{pmatrix}^T \\ \vdots \\ \underbrace{\begin{pmatrix} c_{30}^{-30} & \cdots & c_{30}^0 & \cdots & c_{30}^{30} \end{pmatrix}^T}_{2\times 30+1} \\ \underbrace{\begin{pmatrix} c_{31}^{-31} & \cdots & c_{31}^0 & \cdots & c_{31}^{31} \end{pmatrix}^T}_{2\times 31+1} \\ \vdots \\ \underbrace{\begin{pmatrix} c_{2,\,000}^{-2,\,000} & \cdots & c_{2,\,000}^0 & \cdots & c_{2,\,000}^{2,\,000} \end{pmatrix}^T}_{2\times 2,\,000+1} \end{array} \right)^T. \tag{D7}$$

Each term, c_n^m, in the above equation is a complex number and random numbers are generated by the following two rules:

$$c_n^0 = A_n^0, \tag{D8}$$

$$c_n^m = A_n^m + B_n^m \cdot i,\ c_n^{-m} = (-1)^m \cdot \left(A_n^m + B_n^m \cdot i\right)^*, \tag{D9}$$

where $i^2 = -1$, [ ]* means the conjugate, and A_n^m and B_n^m are real numbers. After c_n is given, it will be used to generate a specific set of SH coefficients, $\mathbb{C}_n$, for the given R_r and D_f by multiplying a real number, P_n, at each raw of c_c,

$$\mathbb{C}_n = \begin{pmatrix} \mathbb{C}_0 \\ \mathbb{C}_1 \\ \mathbb{C}_2 \\ \vdots \\ \mathbb{C}_{30} \\ \mathbb{C}_{31} \\ \vdots \\ \mathbb{C}_{2,\,000} \end{pmatrix}^T = \begin{pmatrix} 2\sqrt{\pi} \\ P_1 \cdot \begin{pmatrix} c_1^{-1} & c_1^0 & c_1^1 \end{pmatrix}^T \\ P_2 \cdot \begin{pmatrix} c_2^{-2} & c_2^{-1} & c_2^0 & c_2^1 & c_2^2 \end{pmatrix}^T \\ \vdots \\ P_{30} \cdot \underbrace{\begin{pmatrix} c_{30}^{-30} & \cdots & c_{30}^0 & \cdots & c_{30}^{30} \end{pmatrix}^T}_{2\times 30+1} \\ P_{31} \cdot \underbrace{\begin{pmatrix} c_{31}^{-31} & \cdots & c_{31}^0 & \cdots & c_{31}^{31} \end{pmatrix}^T}_{2\times 31+1} \\ \vdots \\ \underbrace{P_{2,\,000} \cdot \begin{pmatrix} c_{2,\,000}^{-2,\,000} & \cdots & c_{2,\,000}^0 & \cdots & c_{2,\,000}^{2,\,000} \end{pmatrix}^T}_{2\times 2,\,000+1} \end{pmatrix}^T. \tag{D10}$$

Note that $c_1 = \begin{pmatrix} 0 & 0 & 0 \end{pmatrix}^T$ because it has no evident effects on the grain shape according to Mollon and Zhao (2012) and c_n is kept the same for grains of various R_r and D_f. Further, if n is smaller than the roll-off wavelength at n_r and higher than 1, all real numbers in c_n^m is set to zero: $\underbrace{\begin{pmatrix} c_n^{-n} & \cdots & c_n^0 & \cdots & c_n^n \end{pmatrix}^T}_{2\times n+1} = \underbrace{\begin{pmatrix} 0 & \cdots & 0 & \cdots & 0 \end{pmatrix}^T}_{2\times n+1}$.

Data Availability Statement

Present results and used codes can be found in the Zenodo repository (Zhai, 2023).

Acknowledgments
This work is supported by the National Natural Science Foundation of China (NSFC, Grant 12202342). The authors acknowledge financial supports from Xi'an Jiaotong University, Grants LX6J018 and XZY012021003, and support from the State Key Laboratory for Strength and Vibration of Mechanical Structures, Grant SV2021-KF-28. The first author thanks the Alexander von Humboldt Foundation for supporting his research fellowship at Institute of Geomechanics and Underground Technology, RWTH Aachen University. The first author also thanks and the Australian Research Council (ARC, the Discovery Early Career Award (DECRA), Grant DE240101106) at School of Civil Engineering, The University of Sydney.

References

ABAQUS. (2016). *ABAQUS user's manual, version 2016*. ABAQUS Inc.
Afferrante, L., Carbone, G., & Demelio, G. (2012). Interacting and coalescing Hertzian asperities: A new multiasperity contact model. *Wear*, *278*, 28–33. https://doi.org/10.1016/j.wear.2011.12.013
Aki, K. (1980). Scattering and attenuation of shear waves in the lithosphere. *Journal of Geophysical Research*, *85*(B11), 6496–6504. https://doi.org/10.1029/jb085ib11p06496
Allam, A. A., Kroll, K. A., Milliner, C. W. D., & Richards-Dinger, K. B. (2019). Effects of fault roughness on coseismic slide and earthquake locations. *Journal of Geophysical Research: Solid Earth*, *124*(11), 11336–11349. https://doi.org/10.1029/2018jb016216
Barber, J. (2003). Bounds on the electrical resistance between contacting elastic rough bodies. *Proceedings of the Royal Society of London. Series A: Mathematical, Physical and Engineering Sciences*, *459*(2029), 53–66. https://doi.org/10.1098/rspa.2002.1038
Barrett, P. J. (1980). The shape of rock particles, a critical review. *Sedimentology*, *27*(3), 291–303. https://doi.org/10.1111/j.1365-3091.1980.tb01179.x
Beck, S. L., & Ruff, L. J. (1984). The rupture process of the great 1979 Colombia earthquake: Evidence for the asperity model. *Journal of Geophysical Research*, *89*(B11), 9281–9291. https://doi.org/10.1029/jb089ib11p09281
Ben-David, O., & Fineberg, J. (2011). Static friction coefficient is not a material constant. *Physical Review Letters*, *106*(25), 254301. https://doi.org/10.1103/physrevlett.106.254301
Bhattacharya, P., Rubin, A. M., Tullis, T. E., Beeler, N. M., & Okazaki, K. (2022). The evolution of rock friction is more sensitive to slip than elapsed time, even at near-zero slip rates. *Proceedings of the National Academy of Sciences*, *119*(30), e2119462119. https://doi.org/10.1073/pnas.2119462119
Biegel, R. L., Wang, W., Scholz, C. H., Boitnott, G. N., & Yoshioka, N. (1992). Micromechanics of rock friction 1. Effects of surface roughness on initial friction and slip hardening in westerly granite. *Journal of Geophysical Research*, *97*(B6), 8951–8964. https://doi.org/10.1029/92jb00042
Boitnott, G. N., Biegel, R. L., Scholz, C. H., Yoshioka, N., & Wang, W. (1992). Micromechanics of rock friction 2: Quantitative modeling of initial friction with contact theory. *Journal of Geophysical Research*, *97*(B6), 8965–8978. https://doi.org/10.1029/92jb00019
Borja, R. I. (2013). *Plasticity*. Springer.
Brown, S. R., & Scholz, C. H. (1985a). Broad bandwidth study of the topography of natural rock surfaces. *Journal of Geophysical Research*, *90*(B14), 12575–12582. https://doi.org/10.1029/jb090ib14p12575

Brown, S. R., & Scholz, C. H. (1985b). Closure of random elastic surfaces in contact. *Journal of Geophysical Research*, *90*(B7), 5531–5545. https://doi.org/10.1029/jb090ib07p05531

Bullard, J. W. (2014). Virtual cement and concrete testing laboratory: Version 9.5 user guide, (No Special Publication NIST SP-1173). https://doi.org/10.6028/NIST.SP.1173

Bush, A. W., Gibson, R. D., & Thomas, T. R. (1975). The elastic contact of a rough surface. *Wear*, *35*(1), 87–111. https://doi.org/10.1016/0043-1648(75)90145-3

Byerlee, J. (1978). Friction of rocks. In *Rock friction and earthquake prediction* (pp. 615–626).

Candela, T., Renard, F., Klinger, Y., Mair, K., Schmittbuhl, J., & Brodsky, E. E. (2012). Roughness of fault surfaces over nine decades of length scales. *Journal of Geophysical Research*, *117*(B8), 325. https://doi.org/10.1029/2011jb009041

Carbone, G., & Bottiglione, F. (2008). Asperity contact theories: Do they predict linearity between contact area and load? *Journal of the Mechanics and Physics of Solids*, *56*(8), 2555–2572. https://doi.org/10.1016/j.jmps.2008.03.011

Cattaneo, C. (1938). Sul contatto di due corpi elastici: Distribuzion local degli sforzi. In *Reconditi Accad. naz. Lincei 27, 242–248* (Vol. 434–436, pp. 474–478).

Cavarretta, I., Rocchi, I., & Coop, M. R. (2011). A new interparticle friction apparatus for granular materials. *Canadian Geotechnical Journal*, *48*(12), 1829–1840. https://doi.org/10.1139/t11-077

Ceccato, A., Menegon, L., & Hansen, L. N. (2022). Strength of dry and wet quartz in the low-temperature plasticity regime: Insights from nanoindentation. *Geophysical Research Letters*, *49*(2), e2021GL094633. https://doi.org/10.1029/2021gl094633

Chang, C. S., Chang, Y., & Kabir, M. G. (1992). Micromechanics modeling for stress-strain behavior of granular soils. I: Theory. *Journal of Geotechnical Engineering*, *118*(12), 1959–1974. https://doi.org/10.1061/(asce)0733-9410(1992)118:12(1959)

Ciavarella, M. (1998a). The generalized Cattaneo partial slide plane contact problem. I—Theory. *International Journal of Solids and Structures*, *35*(18), 2349–2362. https://doi.org/10.1016/s0020-7683(97)00154-6

Ciavarella, M. (1998b). The generalized Cattaneo partial slide plane contact problem. II—Examples. *International Journal of Solids and Structures*, *35*(18), 2363–2378. https://doi.org/10.1016/s0020-7683(97)00155-8

Ciavarella, M., Delfine, V., & Demelio, G. (2006). A "re-vitalized" Greenwood and Williamson model of elastic contact between fractal surfaces. *Journal of the Mechanics and Physics of Solids*, *54*(12), 2569–2591. https://doi.org/10.1016/j.jmps.2006.05.006

Cole, D. M., Mathisen, L. U., Hopkins, M. A., & Knapp, B. R. (2010). Normal and sliding contact experiments on gneiss. *Granular Matter*, *12*(1), 69–86. https://doi.org/10.1007/s10035-010-0165-z

Cundall, P. A., & Strack, O. D. (1979). A discrete numerical model for granular assemblies. *Géotechnique*, *29*(1), 47–65. https://doi.org/10.1680/geot.1979.29.1.47

Daly, M. G., Barnouin, O. S., Seabrook, J. A., Roberts, J., Dickinson, C., Walsh, K. J., et al. (2020). Hemispherical differences in the shape and topography of asteroid (101955) bennu. *Science Advances*, *6*(41), eabd3649. https://doi.org/10.1126/sciadv.abd3649

Das, S., & Kostrov, B. V. (1983). Breaking of a single asperity: Rupture process and seismic radiation. *Journal of Geophysical Research*, *88*(B5), 4277–4288. https://doi.org/10.1029/jb088ib05p04277

Das, S., & Kostrov, B. V. (1985). An elliptical asperity in shear: Fracture process and seismic radiation. *Geophysical Journal International*, *80*(3), 725–742. https://doi.org/10.1111/j.1365-246x.1985.tb05121.x

De Dreuzy, J. R., Méheust, Y., & Pichot, G. (2012). Influence of fracture scale heterogeneity on the flow properties of three-dimensional discrete fracture networks (DFN). *Journal of Geophysical Research*, *117*, B11. https://doi.org/10.1029/2012jb009461

Dieterich, J. H. (1979). Modeling of rock friction: 1. Experimental results and constitutive equations. *Journal of Geophysical Research*, *84*(B5), 2161–2168. https://doi.org/10.1029/jb084ib05p02161

Dillavou, S., & Rubinstein, S. M. (2018). Nonmonotonic aging and memory in a frictional interface. *Physical Review Letters*, *120*(22), 224101. https://doi.org/10.1103/physrevlett.120.224101

Dillavou, S., & Rubinstein, S. M. (2020). Shear controls frictional aging by erasing memory. *Physical Review Letters*, *124*(8), 085502. https://doi.org/10.1103/physrevlett.124.085502

Dublanchet, P., Bernard, P., & Favreau, P. (2013). Interactions and triggering in a 3-D rate-and-state asperity model. *Journal of Geophysical Research: Solid Earth*, *118*(5), 2225–2245. https://doi.org/10.1002/jgrb.50187

Elata, D., & Berryman, J. G. (1996). Contact force-displacement laws and the mechanical behavior of random packs of identical spheres. *Mechanics of Materials*, *24*(3), 229–240. https://doi.org/10.1016/s0167-6636(96)00034-8

Erdoğan, S. T., Forster, A. M., Stutzman, P. E., & Garboczi, E. J. (2017). Particle-based characterization of Ottawa sand: Shape, size, mineralogy, and elastic moduli. *Cement and Concrete Composites*, *83*, 36–44. https://doi.org/10.1016/j.cemconcomp.2017.07.003

Gao, H. (1989). Linear perturbation analysis of a shear-loaded asperity. *Journal of Geophysical Research*, *94*(B8), 10259–10266. https://doi.org/10.1029/jb094ib08p10259

Greenwood, J. A., & Tripp, J. H. (1967). The elastic contact of rough spheres. *Journal of Applied Mechanics*, *34*(1), 153–159. https://doi.org/10.1115/1.3607616

Greenwood, J. A., & Williamson, J. P. (1966). Contact of nominally flat surfaces. *Proceedings of the royal society of London. Series A. Mathematical and physical sciences*, *295*(1442), 300–319.

Guo, X., Ma, B., & Zhu, Y. (2019). A magnification-based multi-asperity (MBMA) model of rough contact without adhesion. *Journal of the Mechanics and Physics of Solids*, *133*, 103724. https://doi.org/10.1016/j.jmps.2019.103724

Hertzian, H. (1881). On the contact of elastic solids. *Z. Reine Angew. Mathematik*, *92*, 156–171.

Hsu, C. P., Ramakrishna, S. N., Zanini, M., Spencer, N. D., & Isa, L. (2018). Roughness-dependent tribology effects on discontinuous shear thickening. *Proceedings of the National Academy of Sciences*, *115*(20), 5117–5122. https://doi.org/10.1073/pnas.1801066115

Hyun, S., Pei, L., Molinari, J. F., & Robbins, M. O. (2004). Finite-element analysis of contact between elastic self-affine surfaces. *Physical Review*, *70*(2), 026117. https://doi.org/10.1103/physreve.70.026117

Jäger, J. (1995). Axi-symmetric bodies of equal material in contact under torsion or shift. *Archive of Applied Mechanics*, *65*(7), 478–487. https://doi.org/10.1007/s004190050033

Jäger, J. (1998). A new principle in contact mechanics. *Journal of Tribology*, *120*(4), 677–684. https://doi.org/10.1115/1.2833765

Jenkins, J. T., & Strack, O. D. (1993). Mean-field inelastic behavior of random arrays of identical spheres. *Mechanics of Materials*, *16*(1–2), 25–33. https://doi.org/10.1016/0167-6636(93)90024-l

Jia, X., Caroli, C., & Velicky, B. (1999). Ultrasound propagation in externally stressed granular media. *Physical Review Letters*, *82*(9), 1863–1866. https://doi.org/10.1103/physrevlett.82.1863

Joe, J., Thouless, M. D., & Barber, J. R. (2018). Effect of roughness on the adhesive tractions between contacting bodies. *Journal of the Mechanics and Physics of Solids*, *118*, 365–373. https://doi.org/10.1016/j.jmps.2018.06.005

Johnson, K. L. (1985). *Contact mechanics*. Cambridge University Press.

Kadin, Y., Kligerman, Y., & Etsion, I. (2006). Unloading an elastic–plastic contact of rough surfaces. *Journal of the Mechanics and Physics of Solids*, *54*(12), 2652–2674. https://doi.org/10.1016/j.jmps.2006.04.013
Kasyap, S. S., Senetakis, K., & Zhao, J. (2021). Cyclic normal load–displacement behaviour of clay-coated sand grain contacts. *Géotechnique*, *71*(3), 216–225. https://doi.org/10.1680/jgeot.18.p.216
Kilgore, B., Beeler, N. M., Lozos, J., & Oglesby, D. (2017). Rock friction under variable normal stress. *Journal of Geophysical Research: Solid Earth*, *122*(9), 7042–7075. https://doi.org/10.1002/2017jb014049
Kjartansson, E. (1979). Constant Q-wave propagation and attenuation. *Journal of Geophysical Research*, *84*(B9), 4737–4748. https://doi.org/10.1029/jb084ib09p04737
Komvopoulos, K., & Yang, J. (2006). Dynamic analysis of single and cyclic indentation of an elastic–plastic multi-layered medium by a rigid fractal surface. *Journal of the Mechanics and Physics of Solids*, *54*(5), 927–950. https://doi.org/10.1016/j.jmps.2005.11.010
Lay, T., & Kanamori, H. (1981). An asperity model of large earthquake sequences. *Earthquake prediction: International Review*, *4*, 579–592. https://doi.org/10.1029/me004p0579
Lengiewicz, J., de Souza, M., Lahmar, M. A., Courbon, C., Dalmas, D., Stupkiewicz, S., & Scheibert, J. (2020). Finite deformations govern the anisotropic shear-induced area reduction of soft elastic contacts. *Journal of the Mechanics and Physics of Solids*, *143*, 104056. https://doi.org/10.1016/j.jmps.2020.104056
Li, Q., Tullis, T. E., Goldsby, D., & Carpick, R. W. (2011). Frictional ageing from interfacial bonding and the origins of rate and state friction. *Nature*, *480*(7376), 233–236. https://doi.org/10.1038/nature10589
Li, S., Yao, Q., Li, Q., Feng, X. Q., & Gao, H. (2018). Contact stiffness of regularly patterned multi-asperity interfaces. *Journal of the Mechanics and Physics of Solids*, *111*, 277–289. https://doi.org/10.1016/j.jmps.2017.10.019
Li, S., Zhang, S., Chen, Z., Feng, X. Q., & Li, Q. (2020). Length scale effect in frictional aging of silica contacts. *Physical Review Letters*, *125*(21), 215502. https://doi.org/10.1103/physrevlett.125.215502
Li, Y., Otsubo, M., Kuwano, R., & Nadimi, S. (2021). Quantitative evaluation of surface roughness for granular materials using Gaussian filter method. *Powder Technology*, *388*, 251–260. https://doi.org/10.1016/j.powtec.2021.04.068
Linker, M. F., & Dieterich, J. H. (1992). Effects of variable normal stress on rock friction: Observations and constitutive equations. *Journal of Geophysical Research*, *97*(B4), 4923–4940. https://doi.org/10.1029/92jb00017
Liu, X., & Yang, J. (2018). Shear wave velocity in sand: Effect of grain shape. *Géotechnique*, *68*(8), 742–748. https://doi.org/10.1680/jgeot.17.t.011
Lo, D. S. (2014). *Finite element mesh generation*. CRC Press.
Lorenz, B. (2012). *Contact mechanics and friction of elastic solids on hard and rough substrates* (Vol. 37). Forschungszentrum Jülich.
Lorenz, B., Carbone, G., & Schulze, C. (2010). Average separation between a rough surface and a rubber block: Comparison between theories and experiments. *Wear*, *268*(7–8), 984–990. https://doi.org/10.1016/j.wear.2009.12.029
Luan, B., & Robbins, M. O. (2009). Hybrid atomistic/continuum study of contact and friction between rough solids. *Tribology Letters*, *36*, 1–16. https://doi.org/10.1007/s11249-009-9453-3
Luan, B., & Robbins, M. O. (2021). Friction and plasticity in contacts between amorphous solids. *Tribology Letters*, *69*(2), 1–6. https://doi.org/10.1007/s11249-021-01429-7
Madariaga, R. (1979). On the relation between seismic moment and stress drop in the presence of stress and strength heterogeneity. *Journal of Geophysical Research*, *84*(B5), 2243–2250. https://doi.org/10.1029/jb084ib05p02243
Marone, C., & Cox, S. J. D. (1994). Scaling of rock friction constitutive parameters: The effects of surface roughness and cumulative offset on friction of gabbro. *Pure and Applied Geophysics*, *143*(1–3), 359–385. https://doi.org/10.1007/bf00874335
Melosh, H. J. (1979). Acoustic fluidization: A new geologic process? *Journal of Geophysical Research*, *84*(B13), 7513–7520. https://doi.org/10.1029/jb084ib13p07513
Milliner, C. W., Dolan, J. F., Hollingsworth, J., Leprince, S., Ayoub, F., & Sammis, C. G. (2015). Quantifying near-field and off-fault deformation patterns of the 1992 Mw 7.3 L Anders earthquake. *Geochemistry, Geophysics, Geosystems*, *16*(5), 1577–1598. https://doi.org/10.1002/2014gc005693
Mindlin, R. D. (1949). Compliance of elastic bodies in contact. *Journal of Applied Mechanics*, *16*(3), 259–268. https://doi.org/10.1115/1.4009973
Mindlin, R. D., & Deresiewicz, H. (1953). Elastic spheres in contact under varying oblique forces. *Journal of Applied Mechanics*, *20*(3), 327–344. https://doi.org/10.1115/1.4010702
Misra, A. (1999). Micromechanical model for anisotropic rock joints. *Journal of Geophysical Research*, *104*(B10), 23175–23187. https://doi.org/10.1029/1999jb900210
Mo, Y., Turner, K. T., & Szlufarska, I. (2009). Friction laws at the nanoscale. *Nature*, *457*(7233), 1116–1119. https://doi.org/10.1038/nature07748
Molinari, J. F., Aghababaei, R., Brink, T., Frérot, L., & Milanese, E. (2018). Adhesive wear mechanisms uncovered by atomistic simulations. *Friction*, *6*(3), 245–259. https://doi.org/10.1007/s40544-018-0234-6
Mollon, G., Quacquarelli, A., Andò, E., & Viggiani, G. (2020). Can friction replace roughness in the numerical simulation of granular materials? *Granular Matter*, *22*(2), 1–16. https://doi.org/10.1007/s10035-020-1004-5
Mollon, G., & Zhao, J. (2012). Fourier–Voronoi-based generation of realistic samples for discrete modelling of granular materials. *Granular Matter*, *14*(5), 621–638. https://doi.org/10.1007/s10035-012-0356-x
Monti, J. M., Pastewka, L., & Robbins, M. O. (2022). Fractal geometry of contacting patches in rough elastic contacts. *Journal of the Mechanics and Physics of Solids*, *160*, 104797. https://doi.org/10.1016/j.jmps.2022.104797
Nayak, P. R. (1971). Random process model of rough surfaces (pp. 398–407).
Olsson, E., & Larsson, P. L. (2014). On the tangential contact behavior at elastic–plastic spherical contact problems. *Wear*, *319*(1–2), 110–117. https://doi.org/10.1016/j.wear.2014.07.016
Otsubo, M., & O'Sullivan, C. (2018). Experimental and DEM assessment of the stress-dependency of surface roughness effects on shear modulus. *Soils and Foundations*, *58*(3), 602–614. https://doi.org/10.1016/j.sandf.2018.02.020
Pastewka, L., & Robbins, M. O. (2016). Contact area of rough spheres: Large scale simulations and simple scaling laws. *Applied Physics Letters*, *108*(22), 221601. https://doi.org/10.1063/1.4950802
Pei, L., Hyun, S., Molinari, J. F., & Robbins, M. O. (2005). Finite element modeling of elasto-plastic contact between rough surfaces. *Journal of the Mechanics and Physics of Solids*, *53*(11), 2385–2409. https://doi.org/10.1016/j.jmps.2005.06.008
Persson, B. N. (2006). Contact mechanics for randomly rough surfaces. *Surface Science Reports*, *61*(4), 201–227. https://doi.org/10.1016/j.surfrep.2006.04.001
Persson, P. O., & Strang, G. (2004). A simple mesh generator in MATLAB. *SIAM Review*, *46*(2), 329–345. https://doi.org/10.1137/s0036144503429121

Pohrt, R., & Popov, V. L. (2013). Contact mechanics of rough spheres: Crossover from fractal to Hertzian behavior. *Advances in Tribology*, *2013*, 974178–974184. https://doi.org/10.1155/2013/974178

Putignano, C., Menga, N., Afferrante, L., & Carbone, G. (2019). Viscoelasticity induces anisotropy in contacts of rough solids. *Journal of the Mechanics and Physics of Solids*, *129*, 147–159. https://doi.org/10.1016/j.jmps.2019.03.024

Rockwell, T. K., Dawson, T. E., Young Ben-Horin, J., & Seitz, G. (2015). A 21-event, 4,000-year history of surface ruptures in the Anza seismic gap, San Jacinto Fault, and implications for long-term earthquake production on a major plate boundary fault. *Pure and Applied Geophysics*, *172*(5), 1143–1165. https://doi.org/10.1007/s00024-014-0955-z

Ruina, A. (1983). Slip instability and state variable friction laws. *Journal of Geophysical Research*, *88*(B12), 10359–10370. https://doi.org/10.1029/jb088ib12p10359

Russ, J. C. (2013). *Fractal surfaces*. Springer Science & Business Media.

Sahli, R., Pallares, G., Papangelo, A., Ciavarella, M., Ducottet, C., Ponthus, N., & Scheibert, J. (2019). Shear-induced anisotropy in rough elastomer contact. *Physical Review Letters*, *122*(21), 214301. https://doi.org/10.1103/physrevlett.122.214301

Sandeep, C. S., Marzulli, V., Cafaro, F., Senetakis, K., & Pöschel, T. (2019). Micromechanical behavior of DNA-1A lunar regolith simulant in comparison to Ottawa sand. *Journal of Geophysical Research: Solid Earth*, *124*(8), 8077–8100. https://doi.org/10.1029/2019jb017589

Scheibert, J., Prevost, A., Debrégeas, G., Katzav, E., & Adda-Bedia, M. (2009). Stress field at a sliding frictional contact: Experiments and calculations. *Journal of the Mechanics and Physics of Solids*, *57*(12), 1921–1933. https://doi.org/10.1016/j.jmps.2009.08.008

Sly, M. K., Padilla, K., Flores, K. M., & Skemer, P. (2023). Low-temperature plastic rheology of granitic feldspar and quartz. *Tectonophysics*, *858*, 229850. https://doi.org/10.1016/j.tecto.2023.229850

Song, H., Dikken, R. J., Nicola, L., & Van der Giessen, E. (2015). Plastic ploughing of a sinusoidal asperity on a rough surface. *Journal of Applied Mechanics*, *82*(7), 071006. https://doi.org/10.1115/1.4030318

Song, H., Vakis, A. I., Liu, X., & Van der Giessen, E. (2017). Statistical model of rough surface contact accounting for size-dependent plasticity and asperity interaction. *Journal of the Mechanics and Physics of Solids*, *106*, 1–14. https://doi.org/10.1016/j.jmps.2017.05.014

Song, H., Van der Giessen, E., & Liu, X. (2016). Strain gradient plasticity analysis of elasto-plastic contact between rough surfaces. *Journal of the Mechanics and Physics of Solids*, *96*, 18–28. https://doi.org/10.1016/j.jmps.2016.07.008

Strozewski, B., Sly, M. K., Flores, K. M., & Skemer, P. (2021). Viscoplastic rheology of α-quartz investigated by nanoindentation. *Journal of Geophysical Research: Solid Earth*, *126*(9), e2021JB022229. https://doi.org/10.1029/2021jb022229

Tang, X., & Yang, J. (2021). Wave propagation in granular material: What is the role of particle shape? *Journal of the Mechanics and Physics of Solids*, *157*, 104605. https://doi.org/10.1016/j.jmps.2021.104605

Turcotte, D. L. (1987). A fractal interpretation of topography and geoid spectra on the Earth, moon, venus, and Mars. *Journal of Geophysical Research*, *92*(B4), E597. https://doi.org/10.1029/jb092ib04p0e597

Walsh, J. B., & Brace, W. F. (1984). The effect of pressure on porosity and the transport properties of rock. *Journal of Geophysical Research*, *89*(B11), 9425–9431. https://doi.org/10.1029/jb089ib11p09425

Walsh, J. B., & Grosenbaugh, M. A. (1979). A new model for analyzing the effect of fractures on compressibility. *Journal of Geophysical Research*, *84*(B7), 3532–3536. https://doi.org/10.1029/jb084ib07p03532

Wang, L., Dresen, G., Rybacki, E., Bonnelye, A., & Bohnhoff, M. (2020). Pressure-dependent bulk compressibility of a porous granular material modeled by improved contact mechanics and micromechanical approaches: Effects of surface roughness of grains. *Acta Materialia*, *188*, 259–272. https://doi.org/10.1016/j.actamat.2020.01.063

Wang, W., & Scholz, C. H. (1995). Micromechanics of rock friction: 3. Quantitative modeling of base friction. *Journal of Geophysical Research*, *100*(B3), 4243–4247. https://doi.org/10.1029/94jb02915

Wei, D., Wang, J., Nie, J., & Zhou, B. (2018). Generation of realistic sand particles with fractal nature using an improved spherical harmonic analysis. *Computers and Geotechnics*, *104*, 1–12. https://doi.org/10.1016/j.compgeo.2018.08.002

Wei, D., Wang, Z., Pereira, J. M., & Gan, Y. (2021). Permeability of uniformly graded 3D printed granular media. *Geophysical Research Letters*, *48*(5), e2020GL090728. https://doi.org/10.1029/2020gl090728

Wei, D., Zhai, C., Dorian, H., & Gan, Y. (2020). Contact behaviour of simulated rough spheres generated with spherical harmonics. *International Journal of Solids and Structures*, *193*, 54–68.

Winkler, K. W. (1983). Contact stiffness in granular porous materials: Comparison between theory and experiment. *Geophysical Research Letters*, *10*(11), 1073–1076. https://doi.org/10.1029/gl010i011p01073

Xu, Y., Scheibert, J., Gadegaard, N., & Mulvihill, D. M. (2022). An asperity-based statistical model for the adhesive friction of elastic nominally flat rough contact interfaces. *Journal of the Mechanics and Physics of Solids*, *164*, 104878. https://doi.org/10.1016/j.jmps.2022.104878

Yang, C., & Persson, B. N. J. (2008a). Contact mechanics: Contact area and interfacial separation from small contact to full contact. *Journal of Physics: Condensed Matter*, *20*(21), 215214. https://doi.org/10.1088/0953-8984/20/21/215214

Yang, C., & Persson, B. N. J. (2008b). Molecular dynamics study of contact mechanics: Contact area and interfacial separation from small to full contact. *Physical Review Letters*, *100*(2), 024303. https://doi.org/10.1103/physrevlett.100.024303

Yastrebov, V. A., Anciaux, G., & Molinari, J. F. (2012). Contact between representative rough surfaces. *Physical Review E*, *86*(3), 035601. https://doi.org/10.1103/physreve.86.035601

Yastrebov, V. A., Anciaux, G., & Molinari, J. F. (2015). From infinitesimal to full contact between rough surfaces: Evolution of the contact area. *International Journal of Solids and Structures*, *52*, 83–102. https://doi.org/10.1016/j.ijsolstr.2014.09.019

Yastrebov, V. A., Anciaux, G., & Molinari, J. F. (2017a). On the accurate computation of the true contact-area in mechanical contact of random rough surfaces. *Tribology International*, *114*, 161–171. https://doi.org/10.1016/j.triboint.2017.04.023

Yastrebov, V. A., Anciaux, G., & Molinari, J. F. (2017b). The role of the roughness spectral breadth in elastic contact of rough surfaces. *Journal of the Mechanics and Physics of Solids*, *107*, 469–493. https://doi.org/10.1016/j.jmps.2017.07.016

Yoshioka, N. (1994). Elastic behavior of contacting surfaces under normal loads: A computer simulation using three-dimensional surface topographies. *Journal of Geophysical Research*, *99*(B8), 15549–15560. https://doi.org/10.1029/94jb00938

Zhai, C. (2023). JGR_Frictional contacts between rough grains with fractal morphology [Dataset]. *Zenodo*. https://doi.org/10.5281/zenodo.10219741

Zhai, C., Herbold, E. B., & Hurley, R. C. (2020). The influence of packing structure and interparticle forces on ultrasound transmission in granular media. *Proceedings of the National Academy of Sciences*, *117*(28), 16234–16242. https://doi.org/10.1073/pnas.2004356117

Zhang, F., Liu, J., Ding, X., & Wang, R. (2019). Experimental and finite element analyses of contact behaviors between non-transparent rough surfaces. *Journal of the Mechanics and Physics of Solids*, *126*, 87–100. https://doi.org/10.1016/j.jmps.2019.02.004

Zhao, B. D., Wei, D. H., & Wang, J. F. (2017). Particle shape quantification using rotation-invariant spherical harmonic analysis. *Géotechnique Letters*, *7*(2), 190–196. https://doi.org/10.1680/jgele.17.00011